# Nanoscale Imaging of Phase Transitions with Scanning Force Microscopy

## Citation

Pivonka, Adam. 2012. Nanoscale Imaging of Phase Transitions with Scanning Force Microscopy. Doctoral dissertation, Harvard University.

Thesis advisor Author

**Jennifer E. Hoffman** **Adam Edward Pivonka**

# Nanoscale Imaging of Phase Transitions with Scanning Force Microscopy

## Abstract

Nanoscale imaging of materials through phase transitions can provide valuable insight into the local nature of the transition and the emergence of order. The scanning force microscope used in the studies presented here is an ideal instrument to investigate phase transitions with nanoscale spatial resolution. We study phase transitions in two different systems by operating in different modes: contact mode, in which we measure the local electronic properties of the sample; and non-contact mode, in which we probe the sample by monitoring the interaction between the sample and cantilever.

We increased the versatility of this microscope by developing a method to control the quality factor $Q$ of a conducting cantilever via capacitive coupling to the local environment. We show that $Q$ may be reversibly tuned over a range of a factor of 260. We describe the underlying physics with a point-mass oscillator model. Tuning $Q$ can enhance force-gradient sensitivity or scan speed, which we demonstrate with topographic scans of a $VO_2$ acquired in high vacuum.

Scanning in contact mode with a conductive cantilever, we study local electronic properties of a vanadium dioxide ($VO_2$) thin film through an insulator to metal transition. At each point in the scan, we sweep the voltage applied to the sample, obtaining current versus voltage sweeps with nanoscale resolution while inducing the insulator to metal transition. In some $VO_2$ grains, we see two electronic transitions, consistent with a locally stable intermediate insulating phase. We find large insulating state resistances and transition voltages at grain boundaries, underscoring the importance of Joule heating in triggering the transition in this type of measurement. Finally, we evaluate the conduction mechanism in the insulating regime, allowing the local determination of permittivity and temperature.

We scan in non-contact mode with a magnetic tip to investigate the spin reorientation transition in single-crystal $Nd_2Fe_{14}B$. This ferromagnetic system undergoes the spin reorientation transition near 135 K. We achieve nanoscale magnetic resolution at both room temperature and at a variety of temperatures around the phase transition. We demonstrate the ability to resolve the magnetic domain structure and monitor its evolution through the phase transition.

# Contents

# Acknowledgments

First, I acknowledge the financial support of both the National Science Foundation Graduate Research Fellowship Program and the Fannie and John Hertz Foundation. In addition to financial support, I am grateful to the Hertz Foundation for providing many opportunities to network with other fellows and learn about their research at retreats and symposia.

I would also like to acknowledge my advisor, Professor Jennifer Hoffman. She has been incredibly helpful throughout my time at Harvard, and I greatly appreciate the support, direction, and advice she has provided.

The work in this thesis could not have been completed without the collaborative effort of the MFM team: Lena Huefner, Cun Ye, and Martin Blood-Forsythe. I enjoyed working with all of you, and wish you the best in the future.

My family has been an important part of everything I've done, so I would like to thank Carol Pivonka (my mom), Carl Pivonka (my dad), Dan Pivonka (my brother), and Jim Beitler (my stepfather).

Finally, my fiance, Oana Dan, has been extremely supportive of me as I navigated the ups and downs of graduate school. I am truly lucky to have found her, and I look forward to our future together.

# Chapter 1

# Overview of the Force Microscope

The scanning force microscope used to record the data shown in this thesis is a versatile piece of equipment, enabling the investigation of local properties of samples with nanoscale resolution. The home-built microscope incorporates a fiber optic system to measure the deflection of the cantilever. The cantilever mount supports a variety of cantilevers, enabling operation as both a magnetic force microscope and a traditional atomic force microscope. An electrical connection to the cantilever mount allows measurement of the electrical properties of samples when in contact mode. The microscope is located in a custom-built Janis helium flow cryostat. The system is capable of reaching a base temperature of 4 K. While the turbo pump is running, the vacuum system reaches a base pressure of $10^{-7}$ Torr. A vibration isolation table supports the vacuum system, and the entire system is located inside vibration isolation room resting on a set of air springs. For the work in this thesis, we use the microscope in two modes of operation. In one mode, we place the cantilever in physical contact with the sample. While in contact, we can measure the sample topography while simultaneously sweeping the bias applied to the sample and monitoring the current. In the second mode, we oscillate the cantilever while scanning across the sample surface. Interactions between the cantilever and sample alter properties of the oscillation, such as frequency, amplitude, or phase. Monitoring these changes provides information about the sample, such as magnetic structure or topography.

## 1.1 Vacuum and Cryogenic System

The microscope is contained in a custom-built Janis helium flow cryostat. The nominal base temperature is 1.4 K. However, a leak between the He flow space and the main vacuum space currently prevents operation at temperatures below 4 K. Figure A.4 illustrates the main components of this cryostat. As designed, there are two main spaces in this cryostat: the helium flow space and the vacuum space. The helium flow space forms a concentric region around the vacuum space. When in operation, helium enters the flow space through a needle valve at the bottom of the cryostat. The helium exits the flow space through a pumping port located near the top of the cryostat. Due to the leak in the system, the flow space is physically connected to the vacuum space, and the needle valve has been sealed. The vacuum space, containing the force microscope, is pumped through a 4.5” diameter conflat flange at the top of the cryostat. This conflat flange connects to a six-way cross, which provides connections for the full-range vacuum gauge, optical and electrical feedthroughs, and a turbo pump.

The cryostat is designed to fit within a dewar containing a 5 T superconducting magnet. When not in use, the dewar is stored in a pit below the experiment table. We

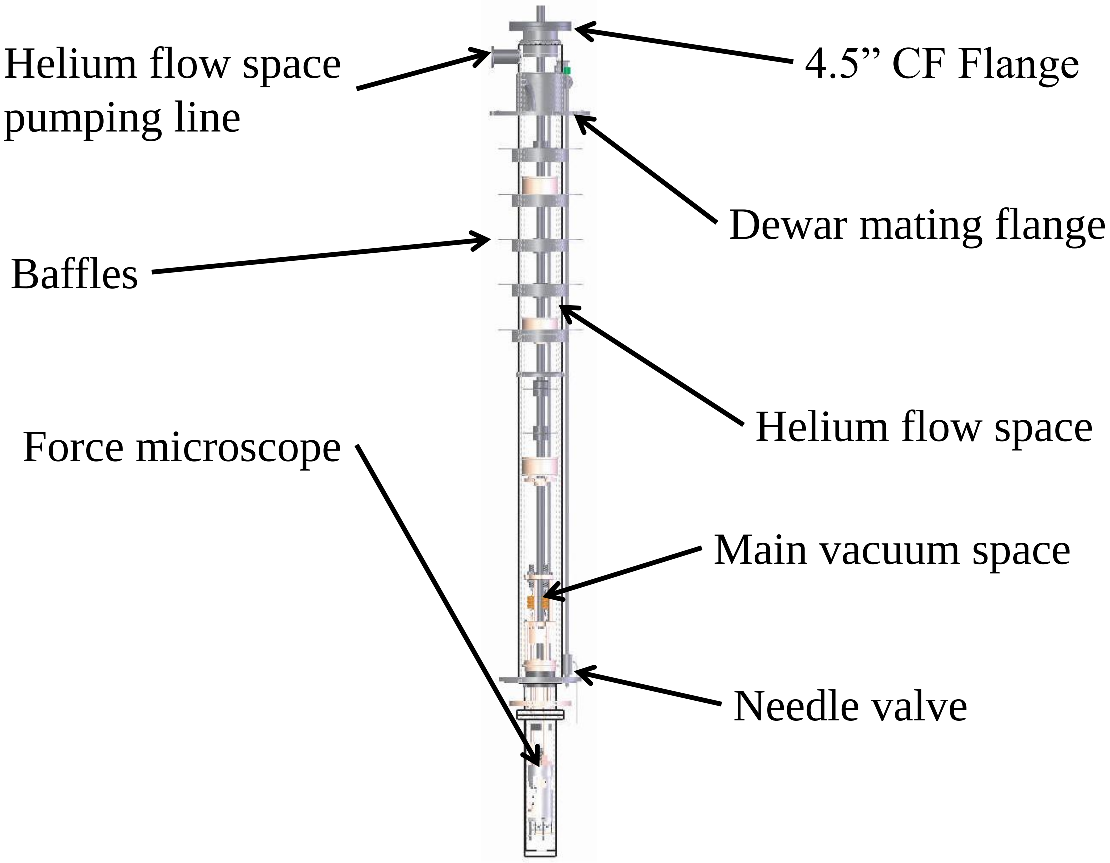

Figure 1.1: Schematic diagram of the flow cryostat.

raise the dewar around the cryostat with a custom lifting system anchored beneath the experiment table. For vibration isolation, the experiment table is filled with 2000 pounds of lead bricks and rests on three air springs. The experiment room itself is supported by six air springs, providing an additional layer of isolation. While imaging, we control the microscope from a room adjacent to the experiment room.

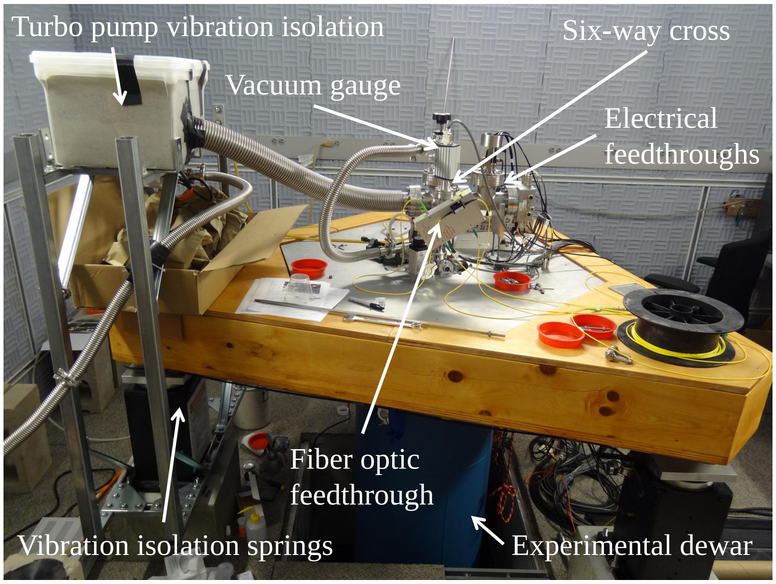

Figure 1.2: Photo of the experimental setup with the dewar raised. The turbo pump is behind the box of sand.

## 1.2 Microscope Head

The microscope head consists of two main components, the cantilever head and the sample head. The cantilever head (Figure 1.3) contains the the fiber optic system and the cantilever. We secure the cantilever with an adjustable spring plate to a cantilever mounting stage, which is rigidly attached to a small piezo stack called the "shake piezo". The shake piezo is driven by an AC signal from the external control electronics. Below the cantilever, the optical fiber protrudes from a ferrule mounted on a commercial piezo stack. This fiber position piezo stack is used to adjust vertical separation between the cantilever and the fiber. A Pan-style walker translates the cantilever laterally relative to the fiber. The initial vertical separation between the fiber and the cantilever must be manually adjusted during alignment by sliding the fiber through the ferrule. Once the separation has been optimized, the fiber is secured in place with a small amount of epoxy.

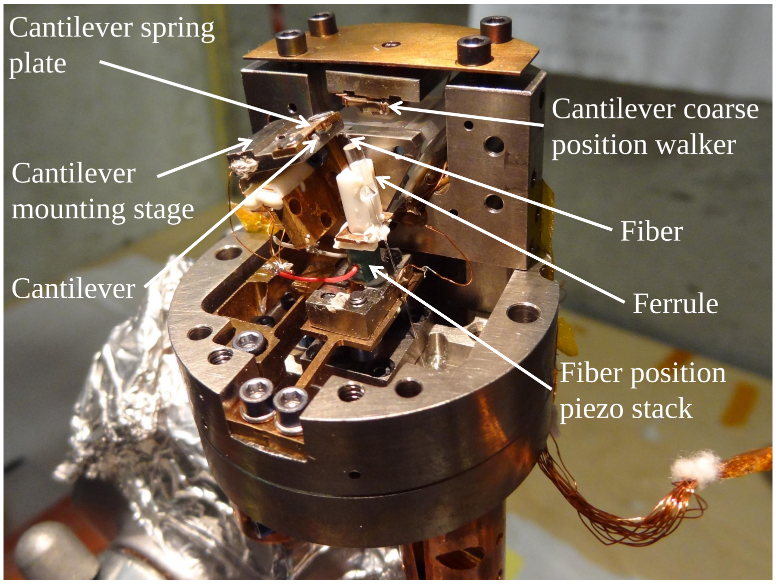

Figure 1.3: Photograph of the cantilever head.

The sample head (Figure 1.4) contains the mounting stage for the sample and the coarse motion mechanisms. The sample is mounted on a sample mounting plate which screws directly into the copper piece glued to the top of the scan piezo. A Cernox temperature sensor and a coil of Manganin wire are also directly attached to this copper piece. The coil of Manganin wire serves as a heater and has a total resistance of 4 Ω. The scan piezo is a four-quadrant piezo tube (EBL-4, 1.5 in. long, 0.25 in. outer diameter, 0.02 in. wall thickness) used to adjust the fine position of the sample relative to the cantilever in all three dimensions. At room temperature in vacuum, the maximum voltage we apply to any quadrant is 150 V, which allows a total scan range of approximately 25 $\mu$m by 25 $\mu$m. We also apply a maximum voltage of 150 V to the center electrode of the scan tube, providing a total vertical range of approximately 2 $\mu$m. A Pan-style walker translates the scan tube and sample to adjust the separation between the cantilever and sample. In addition to the vertical coarse motion system, there are two horizontal coarse positioning systems designed to translate the sample laterally.

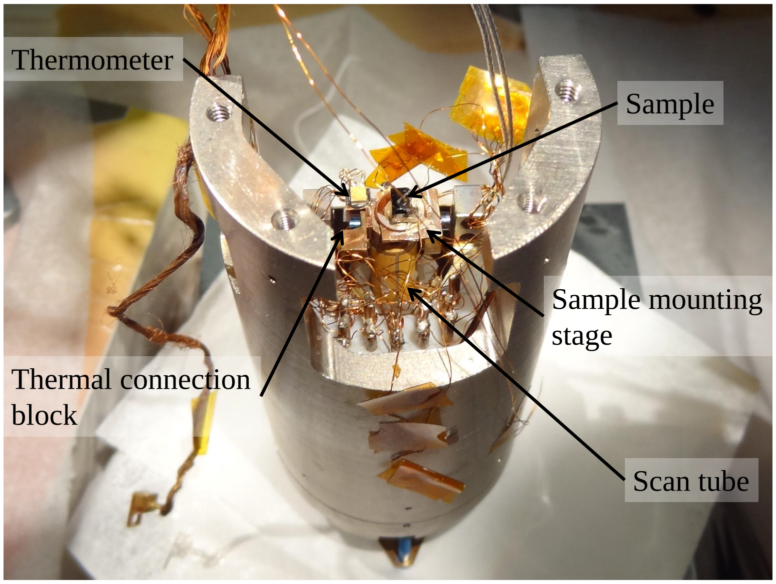

Figure 1.4: Photograph of the sample head.

When in operation the cantilever and sample heads are attached by four screws. The cantilever head is flipped from the configuration shown in Figure 1.3, so the cantilever faces down toward the sample. Figure 1.5 depicts the fully assembled microscope with a scale bar for reference. Figure 1.6 depicts the location of the major components of the microscope head relative to each other while the microscope is assembled.

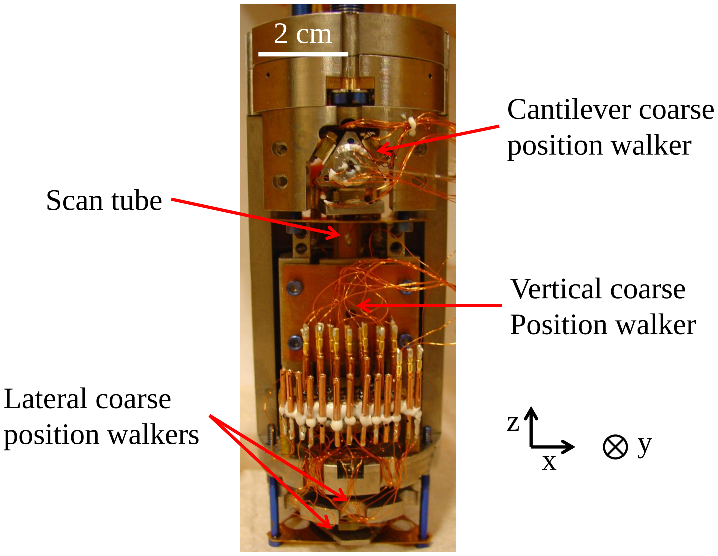

Figure 1.5: Photograph of the fully assembled microscope. The cantilever head attaches to the top of the microscope head.

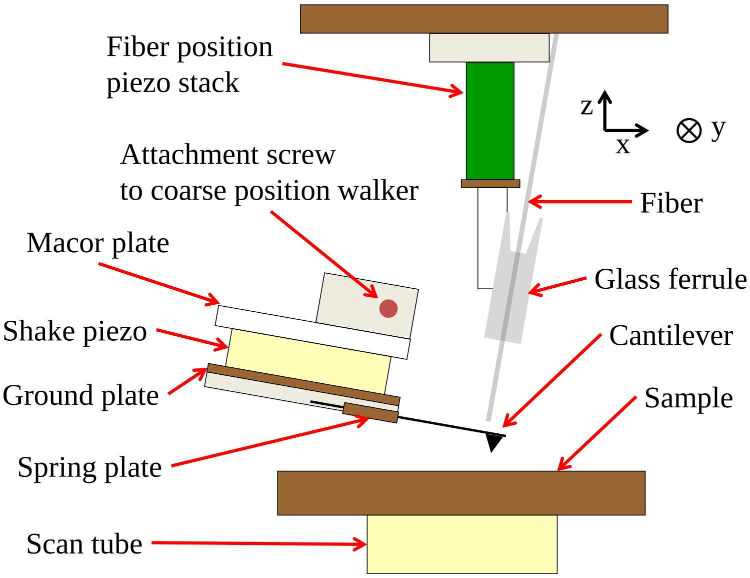

Figure 1.6: Schematic diagram illustrating the main components of the microscope head. The components are not drawn to scale.

## 1.3 Fiber Optic System

In this microscope, an interferometer system is used to detect the deflection of the cantilever. Figure 1.7 provides a schematic overview of this system. Light with a wavelength of 1550 nm from a diode laser (ThorLabs S3FC 1550) passes through an isolator (ThorLabs IO-H-1550) en route to a standard 90/10 2x2 splitter manufactured by Gould Fiber Optics, Inc. At the splitter, 10% of the light enters the vacuum system as the signal beam. This light travels through a single-mode fiber, which ends in a cleaved surface near the cantilever. The interference between the light reflected from the cleaved end of the fiber and that reflected from the cantilever forms the inteferometer signal used to detect the cantilever deflection. The light returning from the inteferometer enters the splitter again, where it is directed to the positive input of a balanced photodetector (New Focus 2117). The remaining 90% of the light forms the reference beam, which is directed through a variable attenuator (ThorLabs VOA50-APC) to the negative input of the photodetector. The attenuator is adjusted so the power in the reference beam matches the average power of the signal beam through a complete interference fringe. Feeding a reference beam of this magnitude to the negative input of the photodetector cancels noise introduced by fluctuations in the laser power.

When the attenuator is properly adjusted, the photodetector output voltage $V_{out}$ is given by

$$V_{out} = \frac{V_{pp}}{2} \cos\left(\frac{4\pi s}{\lambda}\right) \tag{1.1}$$

In this expression, $V_{pp}$ is the peak-to-peak change in output voltage through an interference fringe, $s$ is the separation between the cantilever and fiber, and $\lambda$ is the wavelength of the light. During operation, the separation between the fiber and the cantilever is adjusted to maximize the sensitivity of the interferometer, given by the magnitude of the derivative of the previous expression:

$$\left|\frac{dV_{out}}{ds}\right| = \left|\frac{2\pi V_{pp}}{\lambda}\sin\left(\frac{4\pi s}{\lambda}\right)\right| \tag{1.2}$$

The maximum sensitivity occurs for separations given by $s = \lambda\left(2n+1\right)/8$. When this condition is met, the interferometer sensitivity is given by

$$\left|\frac{dV_{out}}{ds}\right| = \frac{2\pi V_{pp}}{\lambda} \tag{1.3}$$

To increase the sensitivity, $V_{pp}$ must be optimized by aligning the fiber and the cantilever. With careful alignment, $V_{pp}$ can exceed 5 V, corresponding to a sensitivity of 20 mV/nm.

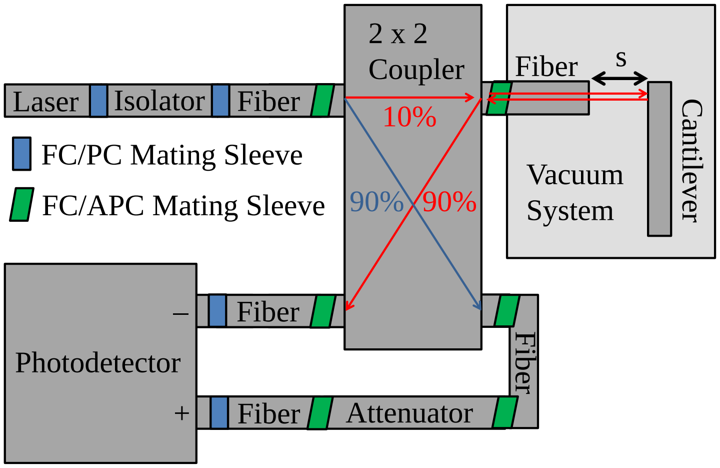

Figure 1.7: Overview of the fiber optic system.

## 1.4 Control Electronics and Software

We control the experiment with a commercial scanning probe microscope controller manufactured by Specs (formerly Nanonis). For our microscope, the control system consists of five electronics boxes (Figure 1.8). The system controls nearly all aspects of the microscope's operation. However, the primary function is to monitor input signals and control feedback loops to keep the signals constant. A variety of signals may serve as inputs to feedback loops, and the controller software allows the user to customize the inputs and outputs based on the goals of the experiment. To this end, the signal conditioning box has both predefined and user-defined inputs and outputs, allowing a great deal of flexibility.

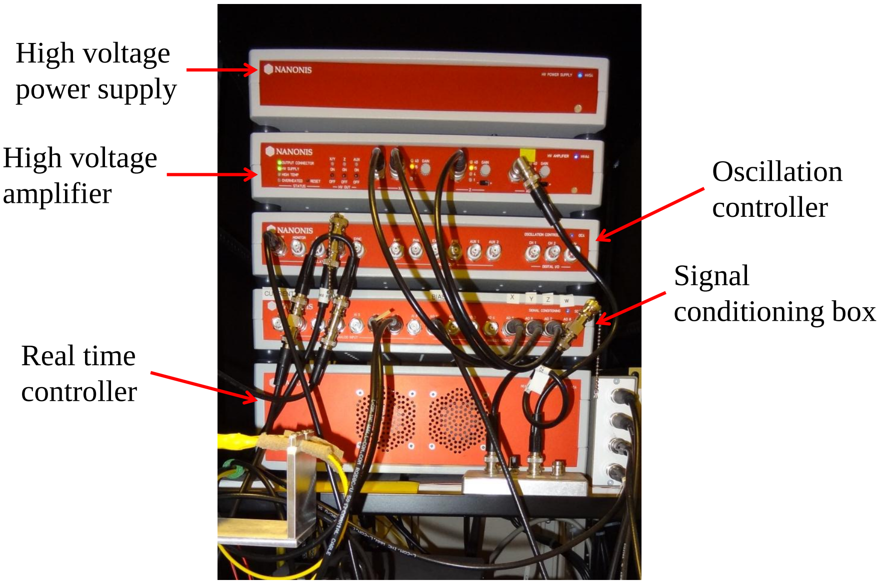

Figure 1.8: Photo of the control electronics system.

One important feedback loop maintains the signal from the interferometer. For maximum interferometer sensitivity, the separation $s$ between the cantilever and the fiber must be kept near $s = \lambda\left(2n+1\right)/8$. To achieve this separation, we sweep the voltage applied to the fiber piezo and note the interferometer signal at the point of maximum slope. This value serves as the set point for the interferometer feedback loop, which controls the separation between the fiber and the cantilever by translating the fiber. This loop operates over time scales much longer than the period of a cantilever's oscillation, so the cantilever oscillation does not affect the feedback loop.

There are three other important feedback loops in addition to the interferometer controller discussed above. First, there is a controller that uses the phase of the cantilever displacement relative to the shake piezo signal as the input to the feedback loop. The feedback setpoint is determined by sweeping the shake piezo drive frequency and monitoring the amplitude and phase of the cantilever's oscillation. Figure 1.9 illustrates the dependence of the oscillation amplitude and phase on drive frequency for a typical cantilever. The phase at the maximum cantilever oscillation amplitude is used as the phase setpoint. The feedback controller attempts to keep this phase constant by varying the shake piezo drive frequency. Another feedback loop uses the cantilever oscillation amplitude as the input signal. In order to maintain constant amplitude, the feedback loop adjusts the amplitude of the signal driving the shake piezo.

Finally, there is the Z-controller. This controller attempts to keep a user-defined setpoint constant by varying the voltage applied to the Z electrode of the scan tube. The controller is quite versatile, as the user can select any input channel to use as the input to the feedback loop. Here, we provide a brief overview of the most commonly-used input signals.

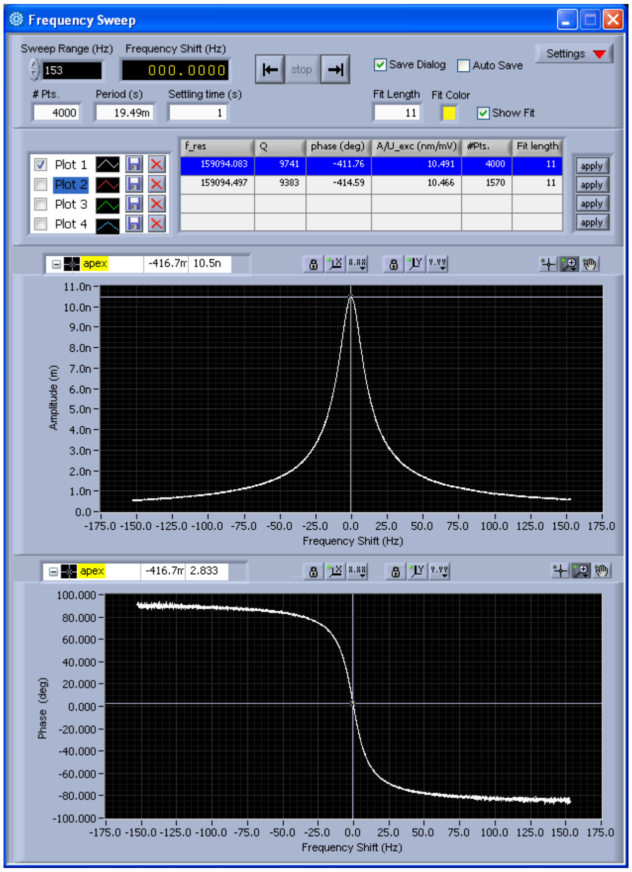

Frequency Sweep

Sweep Range (Hz): 153

Frequency Shift (Hz): 000.0000

☑ Save Dialog ☐ Auto Save

# Pts.: 4000

Period (s): 19.49m

Settling time (s): 1

Fit Length: 11

☑ Show Fit

| | f_res | Q | phase (deg) | A/U_exc (nm/mV) | #Pts. | Fit length |
|---|---|---|---|---|---|---|
| ☑ Plot 1 | 159094.083 | 9741 | -411.76 | 10.491 | 4000 | 11 |
| ☐ Plot 2 | 159094.497 | 9383 | -414.59 | 10.466 | 1570 | 11 |
| ☐ Plot 3 | | | | | | |
| ☐ Plot 4 | | | | | | |

apex: -416.7m, 10.5n

apex: -416.7m, 2.833

Figure 1.9: The dependence of the cantilever oscillation amplitude and phase on the drive frequency for a typical cantilever. The phase at maximum amplitude is used as the setpoint for the feedback loop.

One typical input to the Z-controller is the frequency shift of the cantilever's oscillation, which requires the phase feedback controller to be turned on. In this mode of operation, the interaction between the sample and cantilever causes a shift in the resonance frequency of the cantilever. The phase feedback controller responds to this interaction by shifting the drive frequency to maintain resonance. The shift in drive frequency serves as the input to the Z-controller, which adjusts the separation between the cantilever and the sample. Adjusting this separation changes the interaction between the cantilever and sample. Scanning while the Z-controller is active with a frequency shift set point maps out a contour of constant force gradient between the cantilever and sample. We discuss this interaction in more depth in the following section.

Another possible input to the Z-controller is the oscillation amplitude of the cantilever. In this case, the amplitude controller must be turned off. If the amplitude controller is left active, the Z-controller and amplitude controller will interfere with each other. In the worst case, the Z-controller will attempt to reduce the oscillation amplitude by reducing the separation between the cantilever and the sample. The amplitude controller will simultaneously increase the shake piezo drive amplitude in an attempt to maintain a constant amplitude. The result of this competition may be crashing the cantilever into the surface of the sample, which could damage the sample or destroy the cantilever. If the amplitude controller must be left on for a particular measurement, the Z-controller input can be changed to the shake piezo drive amplitude. In this case, the oscillation amplitude remains constant, and the Z-controller input is a measure of the energy input into the system to maintain constant oscillation amplitude.

Finally, the interferometer signal may be used as the input to the Z-controller. Since the interferometer signal is proportional to the deflection of the cantilever, operating with this input results in the cantilever being physically pressed against the surface. In this mode, the interferometer feedback loop must be inactive. Failure to turn off the interferometer feedback loop may damage the cantilever, as the Z-controller forces the cantilever further into the sample while the interferometer feedback loop maintains constant a constant interferometer signal. Scanning with the interferometer signal as the input can blunt the tip of the cantilever, but it is still useful for a variety of measurements. For example, operating while in contact with a sample using a conductive cantilever allows measurements of the current through the sample as a function of the bias applied to the tip or sample. Scanning in contact can also provide an accurate image of the sample topography, as the interaction between the sample and cantilever is relatively simple.

For many of the feedback loops, the output signal is a voltage used to deform a piezoelectric element. These elements typically require high voltages to deform significantly. The controller system includes a high voltage power supply and amplifier for this purpose. The high voltage amplifier has three independent amplifiers. Two of these control the high voltages applied to the scan tube: one is for the signals to the X and Y electrodes, and one is for the Z electrode. An auxiliary amplifier is available to the user to control another system. In our microscope, the auxiliary amplifier controls the voltage applied to the fiber piezo.

In addition to the controller hardware, the software provides a comprehensive interface to manage experiments and data acquisition. We will provide only an overview of the functionality, as the software allows the user a great deal of flexibility in running an experiment.

One of the most basic functions is sweeping an independent variable and monitoring the input channels. For such a measurement, the user selects the desired parameter to sweep and the channels to monitor during the sweep. In addition to these selections, a user may also choose which feedback loops to remain active during the sweep. We will provide a brief description of two such sweeps. First, one may sweep the bias applied to the Z electrode of the scan piezo and monitor the frequency shift of the cantilever's oscillation. This measurement requires both the phase feedback and interferometer feedback loops to be active. The resulting measurement (called a Z spectroscopy) provides information about the dependence of the frequency shift on the separation between the cantilever and the sample. As we explain in the next section, the frequency shift is proportional to the force gradient of the interaction between the cantilever and sample, so this method provides insight into how the interaction between the sample and cantilever varies with separation. A second example of a sweep is a bias sweep while the cantilever and sample are in contact. For this measurement, the bias applied to the cantilever or sample is swept while monitoring channels such as the current and interferometer signal. To make initial contact with the sample, the Z-controller must use the interferometer signal as an input. However, the Z-controller can be active or inactive during the sweep. Keeping the Z-controller active enables constant contact between the sample and cantilever, while simultaneously measuring changes in the sample topography induced by the application of the current.

The software also enables scanning over the surface of the sample. The user defines the scan parameters, such as the Z-controller input, scan range, and scan speed. In addition, the user selects which channels to record. While there are a great variety of scans that are possible, we describe a measurement of the sample topography as an example. For a typical topography, the interferometer and phase feedback controllers would be active, and the Z-controller input would be the frequency shift. During the scan, one may choose to monitor the frequency shift, phase, and Z position. The frequency shift and phase channels would serve as diagnostic checks to confirm that the feedback loops operated correctly. Ideally, both the frequency shift and phase channels would contain no structure; that is, they would only contain constant values equal to the set points for the feedback loops. In practice, abrupt changes in the surface topography, surface contamination, and rapid scan speeds may prevent the feedback loops from maintaining input values equal to the setpoint. The Z position channel contains the desired topographic information.

Finally, the software enables performing sweeps of an independent variable while scanning across the surface. As before, the user is free to define the independent variable to sweep and the channels to measure during the sweep. For a measurement such as this, the data set consists of a grid of points across the sample surface, each with an associated sweep. To further customize these measurements, the software allows the user to incorporate their own LabVIEW code. For example, we have used this functionality to customize the data collection for a grid of bias sweep measurements. For these measurements, it is desirable to lift the cantilever from the surface while traveling from point to point to reduce damage to the tip. While lifted, we change the Z-controller settings to acquire topographic information about the sample using the frequency shift signal as the input to the Z-controller. The cantilever then moves to the next position, the Z-controller input is changed back to the interferometer signal, the cantilever contacts the surface, and a series of bias sweep measurements are taken. The control electronics and associated software enable a broad range of measurements through the combination of built-in functions and the ability to incorporate customized code written by the user.

## 1.5 Operating Modes

### 1.5.1 Overview

For the work in this thesis, we operate in two separate modes: contact mode and non-contact mode. By “non-contact,” we refer to a regime where the cantilever is free to oscillate. In other words, the cantilever may be in intermittent contact with the surface, but oscillating the cantilever results in a measurable oscillation amplitude. By “contact,” we refer to a regime where contact between the cantilever and sample is not in question. In this case, the cantilever is physically pressed against the surface, causing cantilever deflection.

### 1.5.2 Non-contact mode

Far away from the surface, the motion of the cantilever can be described by the damped, driven harmonic oscillator equation.

$$m\ddot{z} + b\dot{z} + k\left(z - z_0\right) = Fe^{i\omega t} \tag{1.4}$$

In this expression, $m$ is the effective mass of the cantilever, $b$ is the damping coefficient, $k$ is the effective spring constant of the cantilever, and $z$ is the displacement of the cantilever, and $z_0$ is the equilibrium position of the cantilever. Here, the cantilever is driven by a periodic force $Fe^{i\omega t}$, which is transduced from the oscillation of the piezo stack attached to the cantilever mounting stage.

The resonance frequency $\omega_r$ is given by

$$\omega_r = \sqrt{\frac{k}{m}}\sqrt{1-\frac{b^2}{2mk}} \tag{1.5}$$

However, for typical cantilevers, $\frac{b^2}{2mk} << 1$, and we can approximate the resonance frequency as $\omega_r \approx \sqrt{\frac{k}{m}}$. When the cantilever and sample are in close proximity, there is a force $F_{TS}\left[z\right]$ between them. For small cantilever oscillations, we can approximate this force with a Taylor series expansion around the cantilever's equilibrium displacement.

$$F_{TS}\left[z\right] = F_{TS}\left[z_0\right] + \frac{dF_{TS}}{dz}\left(z-z_0\right) + ... \tag{1.6}$$

Inserting this expression into the equation of motion for the cantilever gives

$$m\ddot{z} + b\dot{z} + k\left(z-z_0\right) = Fe^{i\omega t} + \frac{dF_{TS}}{dz}\left(z-z_0\right) \tag{1.7}$$

We have ignored the term $F_{TS}\left[z_0\right]$, because its sole effect is to shift the equilibrium position $z_0$ of the cantilever. Rearranging the terms, we have

$$m\ddot{z} + b\dot{z} + \left(k - \frac{dF_{TS}}{dz}\right)\left(z-z_0\right) = Fe^{i\omega t} \tag{1.8}$$

From this expression, we observe that we can define an effective spring constant incorporating the gradient of the force between the cantilever and sample

$$k_{eff} = \left(k - \frac{dF_{TS}}{dz}\right) \tag{1.9}$$

Thus, in the presence of a force gradient, the resonance frequency of the cantilever becomes

$$\omega_r' = \sqrt{\frac{k_{eff}}{m}} \tag{1.10}$$

When the force gradient is small relative to the cantilever spring constant, or $\frac{dF_{TS}}{dz} << k$, then we can approximate the shift in resonance frequency with the binomial approximation

$$\frac{\omega_r' - \omega_r}{\omega_r} = \frac{\Delta\omega_r}{\omega_r} \approx -\frac{1}{2k}\frac{dF_{TS}}{dz} \tag{1.11}$$

We see that for small force gradients, the shift in resonance frequency is proportional to the force gradient itself. For the work presented here, we primarily use cantilevers with native resonance frequencies of around 70 kHz or 160 kHz. In each case, we typically scan with frequency shift values on the order of 10 to 100 Hz, indicating the small force gradient approximation is valid.

While near the surface, we can choose to scan with the Z-controller active or inactive. These two techniques provide complementary information. With the Z-controller feedback loop inactive, the cantilever is scanned over the surface at a constant height. For constant height scans, the frequency shift channel contains information about the local gradient of the force between the sample and cantilever, while the Z position channel contains no information (aside from the height of the scan, which is just a number). Thus, constant height scans can be interpreted as maps of the force gradient at a given height. These scans can be particularly useful for samples that have large variations in the interaction between the sample and cantilever across the surface or those for which it is difficult to achieve stable feedback due to surface contamination.

With the Z-controller feedback active, the height of the cantilever above the surface adjusts to maintain a constant frequency shift. In this case, the frequency shift channel serves as a diagnostic tool for evaluating the Z-controller feedback loop. If the data in this channel deviates significantly from the Z-controller setpoint, the Z-controller feedback settings may not be optimized or the scan speed may be too fast. The Z position channel records the separation between the cantilever and sample required to keep the frequency shift constant at the set point. A map of the Z position thus shows a contour of constant force gradient between the cantilever and the sample. Scans of this type can be referred to as a topography, but this distinction should be noted.

### 1.5.3 Contact Mode

In contact mode, the cantilever does not oscillate. Instead, it is pressed directly into the surface of the sample by using the interferometer signal as the input to the Z-controller. The interferometer signal is proportional to the cantilever displacement, so the setpoint determines the degree to which the cantilever deflects as it makes contact with the surface. A typical setpoint may be 100 mV above the value observed with no cantilever deflection. For an interferometer sensitivity of 20 nm/V, this corresponds to a cantilever deflection of approximately 5 nm while in contact. For a typical cantilever with a spring constant of 40 N/m, the force applied to the sample by the cantilever is approximately 200 nN. Scanning across the surface with the Z-controller active produces a topography of the sample surface.

Contact mode is most useful with a conductive cantilever and sample installed. When both the sample and cantilever are conductive, the physical contact between the two allows local measurements of the current through the sample as a function of the bias applied to either the cantilever or the sample. One method of scanning is to apply a constant bias to the sample while performing a standard scan in contact mode. Monitoring the current channel in this configuration produces a map of the current at the particular applied bias. This approach has the advantage of being quite fast. Another, more comprehensive, approach is to sweep the applied bias at every location in a grid across the sample. This provides the full dependence of the current on the applied bias across the sample, as well as any additional information that may be recorded, such as the Z position or interferometer signal during the sweep.

In the next chapter, we discuss a method to tune the quality factor $Q$ of a conducting cantilever. This technique is useful when operating in the non-contact scanning mode described above. In the third chapter, we explore the local electronic properties of a thin film of $VO_2$, which relies on bias sweeps carried out while scanning in contact mode. In the final chapter, we image the magnetic domain structure of $Nd_2Fe_{14}B$ by operating in non-contact mode using cantilevers with tips sensitive to magnetic fields. To confirm that the features we see are magnetic in nature, we also scan in contact mode to determine the sample topography.

# Chapter 2

# Q Control

## 2.1 Introduction

While the atomic force microscope (AFM) [4] is a powerful tool for nanoscale imaging [29], manipulation [44, 54], and fabrication [13, 26], many externally imposed constraints limit the choice of its measurement parameters. For example, sample decay, image distortion due to thermal or piezo drift, and limited cryogen hold time all restrict the duration of data collection. Additionally, sensitive samples may place upper bounds on the imaging force.

Cantilever quality factor ($Q$) control has been one popular method for circumventing some of these constraints. Since $Q$ is a measure of the energy dissipated in each oscillation cycle, it is proportional to the transient response time $\tau = Q/(\pi f_c)$, where $f_c$ is the cantilever resonance frequency [2]. Thus, $Q$ reduction has been used to increase the bandwidth of the AFM for faster imaging in vacuum [49, 47, 35, 12]. Conversely, $Q$ enhancement can improve force sensitivity and reduce the average contact force applied to fragile samples in tapping mode [51, 17, 43, 23]. Phase contrast [16] and force gradient sensitivity [23, 22, 6] may also be increased.

Cantilever $Q$ control has previously been achieved via active damping [28, 9] or parametric excitation [45]. Most implementations of $Q$ control are realized by means of "self-excitation", in which a feedback signal is added directly to the original signal driving the cantilever. Active damping has also been demonstrated using state feedback control [47, 35] and a variety of secondary driving forces such as photothermal forces [28] and radiation pressure [53].

Here, we report a simple capacitive coupling technique that can be used to tune a cantilever's $Q$ by a factor of up to 260, depending on the native $Q$ of the cantilever. We demonstrate this $Q$ control experimentally and describe the dynamics of the system with a point-mass oscillator model, which we show to be consistent with the experimentally observed behavior. Since the effect relies on capacitive coupling between the cantilever and the environment, the only requirement is that the cantilever be conductive and in close proximity to a conductive environment whose voltage $V_s$ can be set independently. The method can typically be employed quickly and cheaply, without modifying the AFM head.

## 2.2 Experimental Methods

An overview of the experimental setup is provided in Figure 2.1. Light from the 1550 nm diode laser enters the system via a single mode optical fiber. This light is partially reflected from the end of the cleaved fiber and partially from the cantilever, leading to an interference signal proportional to the displacement of the cantilever.

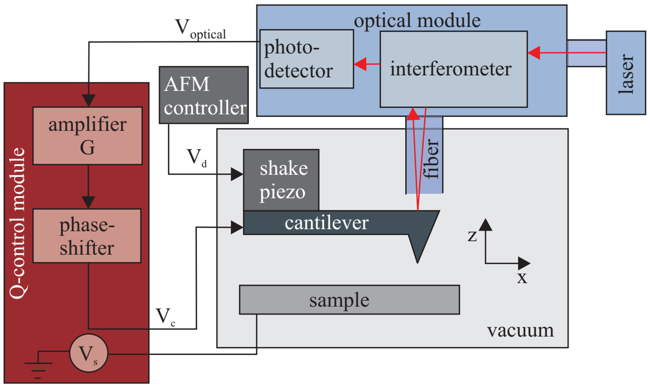

Figure 2.1: Schematic diagram of the experimental setup. The $Q$ control module (red) may be added without breaking vacuum (grey) or modifying the existing optical circuitry (blue).

The balanced photodetector converts the interference signal to a voltage, $V_{\text{optical}}$.

A periodic drive signal $V_d$ deforms a "shake" piezo to oscillate the cantilever. We acquire resonance curves by sweeping the drive frequency $f_d$ while recording both the amplitude and phase of the cantilever's motion relative to the drive. We determine the quality factor via $Q = pf_c/2$, where $p$ is the measured slope of the phase versus $f_d$ in the linear region centered about $f_c$. Consecutive $Q$ measurements under nominally identical conditions are repeatable to within $\sim 5\%$. We have therefore rounded all reported $Q$ values to the nearest hundred.

To modify $Q$, we use a commercial amplifier (Stanford Research Systems SR560) to enhance $V_{\text{optical}}$ by a unitless gain factor $G$. We then phase shift the signal by 90° relative to the cantilever displacement via a homebuilt phase shifter. The resulting voltage $V_c$ is applied directly to the cantilever. For periodic oscillations, $V_c$ is proportional to the velocity of the cantilever, and can be expressed as $V_c = \left(\frac{sG}{2\pi f_d}\right)\dot{z}$, where $s$ is the sensitivity of the interferometer. An additional DC voltage $V_s$ is applied to the sample with respect to the cantilever. $G$ and $V_s$ may be tuned independently to change $Q$.

## 2.3 Modeling Q

Understanding the dependence of $Q$ on $G$ and $V_s$ requires modeling. Far from the sample, the equation of motion for the cantilever is

$$m\ddot{z} + b\dot{z} + kz = F\cos\left(2\pi f_d t\right) + \frac{\gamma}{2}\left(V_c - V_s\right)^2, \tag{2.1}$$

where $m$ is the effective mass of the cantilever, $z$ is the displacement normal to the sample surface (see Figure 2.1), $b$ is the damping coefficient, $k$ is the spring constant, $F$ is the driving force amplitude (proportional to $V_d$), $t$ is the time, and $\gamma \equiv dC/dz$ is the derivative of the cantilever-environment capacitance $C$ with respect to cantilever-sample separation. $V_s$ and $V_c$ are the voltages applied to the sample and cantilever, respectively. Substituting $V_c = \left(\frac{sG}{2\pi f_d}\right)\dot{z} \equiv g\dot{z}$, we have

$$m\ddot{z} + \left(b + \gamma g V_s\right)\dot{z} + kz = F\cos\left(2\pi f_d t\right) + \frac{\gamma g^2}{2}\dot{z}^2. \tag{2.2}$$

We have ignored a constant term proportional to $V_s^2$, corresponding to a small, constant shift of $\sim 10^{-2}\,\mathrm{nm}$ in the equilibrium displacement of the cantilever. Eq. 2.2 differs from the standard damped, driven oscillator only in the final nonlinear term.

Note that the substitution of $g\dot{z}$ for $V_c$ is an approximation. The validity of the approximation is limited by our ability to adjust the phase of $V_c$ ($\pm 10°$), by the frequency response of the phase shifter, and by the possible non-sinusoidal oscillations introduced by the nonlinear term, $\gamma g^2\dot{z}^2/2$. However, we will show that this model describes the measured motion of the cantilever well near the resonance frequency.

Note that in the absence of the nonlinear term, $Q^{-1}$ depends linearly on $G$ and $V_s$ via the following relation:

$$Q^{-1} = \underbrace{\frac{b}{2\pi f_c m}}_{\equiv \beta} + \underbrace{\frac{\gamma s}{m(2\pi f_c)^2}}_{\equiv \Gamma} G \cdot V_s, \tag{2.3}$$

where $f_c$ is the natural resonance frequency of the free cantilever, and we have used $f_d \approx f_c$ near resonance.

To investigate the effects of the nonlinear term, we model the motion of the cantilever using MATLAB's built-in ordinary differential equation solver, ODE45, to determine the oscillation amplitude and phase relative to $V_d$ from the full Eq. 2.2. In analogy to the experiment, $Q$ is extracted from the modeled dependence of the relative phase on the drive frequency in the linear region around resonance.

In order to effectively compare the results obtained from modeling to those obtained experimentally, we require reasonable estimates for the model input parameters. We obtain the values of these parameters using a variety of methods. The measured resonance curve with the cantilever in the native state provides the resonance frequency $f_c$, amplitude at resonance $\alpha$, and quality factor $Q_n$. The spring constant $k$ is available from information provided by the manufacturer, albeit with high uncertainty. We calculate the damping coefficient $b$ using $b = k/(2\pi f_c Q_n)$ and the effective mass $m$ of the cantilever using $m = k/\left(2\pi f_C\right)^2$. We determine the force $F$ transduced from the shake piezo drive signal $V_d$ using $F = \alpha k/Q_n$. Finally, we determine the value of the capacitive coupling parameter $\gamma$ by fitting the dependence of cantilever deflection on $V_s$. The coefficient to the quadratic term in the fit is $\eta = s\gamma/2k$. $m$, $b$, $F$, and $\gamma$ all have large uncertainties, which they inherit from the

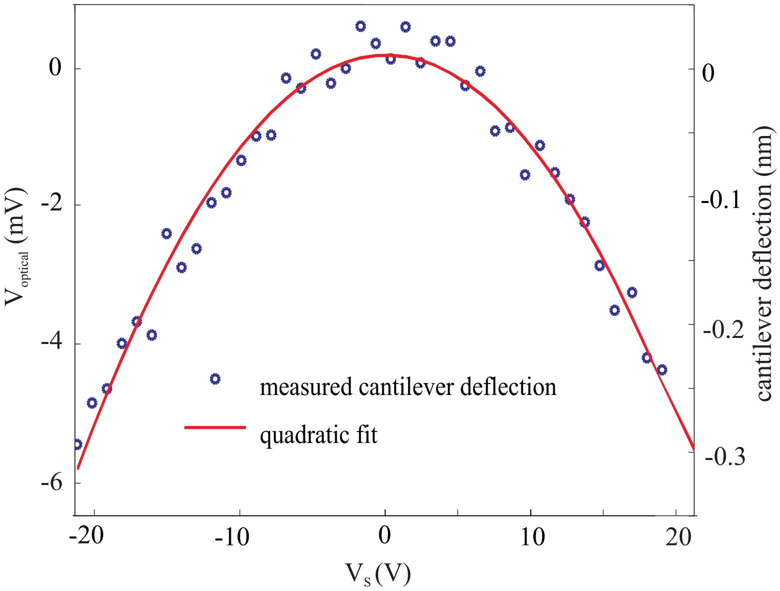

Figure 2.2: Measured cantilever deflection as a function of $V_s$, for cantilever A. For each measured value of $V_{\text{optical}}$ (blue dot), both $V_d = 0$ and $V_c = 0$, i.e. there was no time-varying force from either the capacitive coupling or the shake piezo. While $V_{\text{optical}}$ is the directly measured quantity, we compute and display cantilever displacement on the right axis, using the measured value of $s$. The quadratic fit to $V_{\text{optical}}$ vs. $V_s$ (red line) is used to determine the capacitive coupling parameter $\gamma$ from the coefficient to the second order term, $\eta = s\gamma/2k$.

uncertainty in $k$. However, the only term that enters directly into the model is $\eta$, which we measure independently. In Figure 2.2, we show example cantilever deflection data and the corresponding fit. The value for $\eta$ is determined by calculating the mean and standard deviation of the quadratic coefficient of the fits of 48 deflection curves. Table 2.1 provides an overview of the values, uncertainties, and methods of obtaining the input parameters to our model.

To model the behavior of the oscillation using computational methods, we cast Eq. 2.2 into a dimensionless form,

$$\ddot{y} = \cos(B\tau) + C\dot{y}^2 - A\dot{y} - y. \tag{2.4}$$

Table 2.1: Values of the model input parameters for cantilever A and the methods we use to obtain them. The primary source of uncertainty in many of the parameters is the uncertainty in the cantilever spring constant provided by the manufacturer. However, we obtain $\eta$, the most important term in the model, through an independent measurement.

| Parameter | Value | Uncertainty | Method to obtain |
|---|---|---|---|
| $k$ | $40\,\mathrm{N/m}$ | $+150\%/-60\%$ | Cantilever manufacturer |
| $f_c$ | $160,970\,\mathrm{Hz}$ | $\pm 1\,\mathrm{Hz}$ | Measured from resonance sweep |
| $Q_n$ | $16,000$ | $\pm 160$ | Calculated from $Q_n = pf_c/2$ |
| $\eta$ | $-1.13 \times 10^{-5}\,\mathrm{V}^{-1}$ | $\pm 0.11 \times 10^{-5}\,\mathrm{V}^{-1}$ | Quadratic fit coefficient from cantilever deflection curve; reported value and uncertainty are the mean and standard deviation from 48 independently measured curves, a single example of which is shown in Figure 2.2 |
| $m$ | $4 \times 10^{-11}\,\mathrm{kg}$ | $+150\%/-60\%$ | Calculated from $m = k/\left(2\pi f_C\right)^2$ |
| $b$ | $2 \times 10^{-9}\,\mathrm{kg/s}$ | $+150\%/-60\%$ | Calculated from $b = k/(2\pi f_c Q_n)$ |
| $\alpha$ | $21.3\,\mathrm{nm}$ | $\pm 0.1\,\mathrm{nm}$ | Measured from resonance sweep |
| $F$ | $50\,\mathrm{pN}$<br>(for $V_d = 0.5\,\mathrm{mV}$) | $+150\%/-60\%$ | Calculated from $F = \alpha k/Q_n$ |
| $s$ | $1.9 \times 10^{7}\,\mathrm{V/m}$ | $\pm 0.1 \times 10^{7}\,\mathrm{V/m}$ | Measured by sweeping the cantilever-fiber separation through a full interference fringe |
| $\gamma$ | $-5 \times 10^{-11}\,\mathrm{C/(V \cdot m)}$ | $+150\%/-60\%$ | Calculated from $\gamma = 2k\eta/s$ |

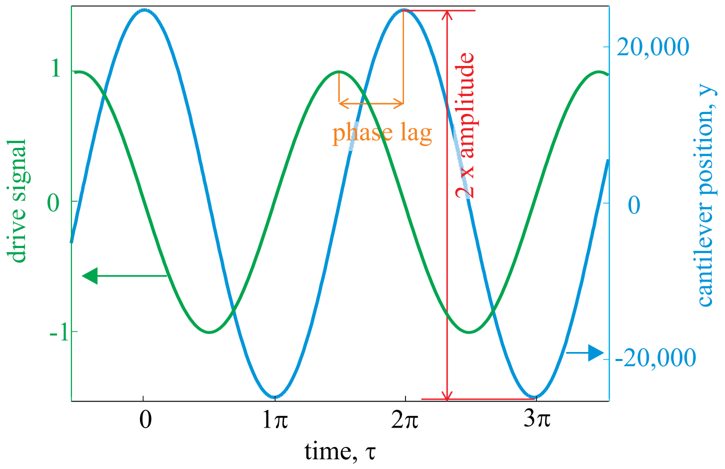

Figure 2.3: Modeled drive signal and position of the cantilever versus time. The signals are plotted well into the steady-state regime.

In this equation, $A = (Q_n^{-1} + 2\eta G V_s)$, $B = f_d/f_c$, $C = \eta \alpha s G^2/Q_n$, $y = zQ_n/\alpha$, and derivatives are taken with respect to the dimensionless time $\tau = 2\pi f_c t$. With this dimensionless equation, we use MATLAB to model the oscillation of the cantilever as a function of the input parameters, $A$, $B$, and $C$. For each set of inputs, we calculate the steady-state oscillation amplitude of the cantilever and the phase of the oscillation relative to the drive signal. In Figure 2.3, we plot an example of the drive signal and the position of the cantilever for a particular parameter set ($A = 4 \times 10^{-5}$, $B = 1$, $C = 2.86 \times 10^{-10}$, corresponding to $G = 1$ and $V_s = 1\,\mathrm{V}$). We determine that the oscillation amplitude is $24,900$ (red arrow), and the relative phase between the curves is $(0.50 \pm 0.01)\,\pi$ (orange arrow).

We simulate a resonance curve measurement by sweeping the normalized frequency $B$, while holding $A$ and $C$ constant at the same values used to produce Figure 2.3. In Figure 2.4, we show the resonance curve and the associated phase dependence on the drive frequency obtained using the model. We determine the quality factor via

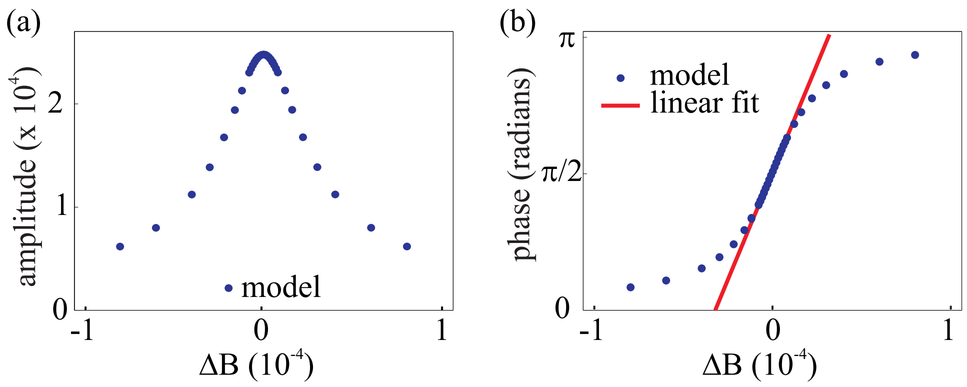

Figure 2.4: Modeled cantilever oscillation amplitude (a) and relative phase (b) as a function of relative drive frequency $\Delta B = B - 1$. We determine $Q$ from a linear fit to the relative phase (shown in red).

$Q = pf_c/2$, where $p$ is the measured slope of the phase versus $B$ in the linear region centered about resonance. From the plots in Figure 2.4, we find $Q = 24,500$.

## 2.4 Results and Discussion

We demonstrate reliable $Q$ control using a variety of cantilevers and samples, detailed in Table 2.2. All data shown in the figures were recorded under the following conditions. The AFM was at room temperature in high vacuum ($\sim 10^{-7}$ torr). The sample was a $\sim$ 100 nm thick $VO_2$ film grown on a highly doped Si substrate. The shake piezo drive amplitude was 0.5 mV peak-to-peak unless otherwise noted. For Figures 2.5-2.6 the cantilever-sample separation was fixed at 1 $\mu$m, and results were found to be independent of the lateral position of the cantilever.

Figure 2.5 demonstrates the dependence of $Q$ on $V_s$ and $G$. In Figure 2.5 (a,b), we show the effect of varying $V_s$ for fixed $G = 1$. Increasing $V_s$ simultaneously increases the height of the resonance peak and the slope of the phase plot, while decreasing

$V_s$ has the opposite effect. Tuning $V_s$ therefore allows for both enhancement and reduction of $Q$. In Figure 2.5 (c-f) we show the effect of varying $G$ for both positive and negative $V_s$. Increasing $G$ with negative $V_s$ results in $Q$ reduction [Figure 2.5 (c,d)], while increasing $G$ with positive $V_s$ leads to $Q$ enhancement [Figure 2.5 (e,f)].

Table 2.2: Native $Q$ ($Q_n$), as well as the minimum and maximum $Q$ for a variety of cantilevers and samples.

| Cantilever Description | Sample | $Q_n$ | $Q_{\mathrm{min}}$ | $Q_{\mathrm{max}}$ |
|---|---|---|---|---|
| A. $\mu$masch NSC 16 | $VO_2$ | 16,000 | 3,200 | 142,100 |
| B. $\mu$masch NSC 16 | $VO_2$ | 13,700 | 1,400 | 92,000 |
| C. $\mu$masch NSC 18 | $NdFeAsO_{1-x}F_x$ | 8,400 | 600 | 8,400 |
| D. Nanosensors TL CONT | hard drive | 100,000 | 400 | 104,000 |
| E. Nanosensors SSS QMFMR | hard drive | 21,000 | 1,800 | 428,600 |

We compare our experimental results with those obtained from the model by investigating the dependence of $Q^{-1}$ on both $V_s$ and $G$ [Figure 2.6]. Experimentally, we observe that $Q^{-1}$ depends linearly on both the amplifier gain and the sample voltage for a large range of $Q$ [Figure 2.6 (c,d)]. For $Q$ below about $5,000$ the precision with which we can determine $Q$ decreases as a result of the weak dependence of both the oscillation amplitude and the phase of the cantilever on $f_d$. This is apparent from the raw data displayed in Figure 2.5. At the high $Q$ end of the range, typically around $\sim 150,000$, we find that the oscillation can become unstable and self-reinforcing, leading to the continued oscillation of the cantilever at large amplitude even in the absence of the external driving force. In our model, this instability occurs when the damping coefficient, $b + \gamma g V_s$, becomes negative. Within these limits, our model reproduces the experimentally determined slope of $Q^{-1}$ to within 25% of the experimental value. This discrepancy in $\Gamma$ between model and experiment falls within

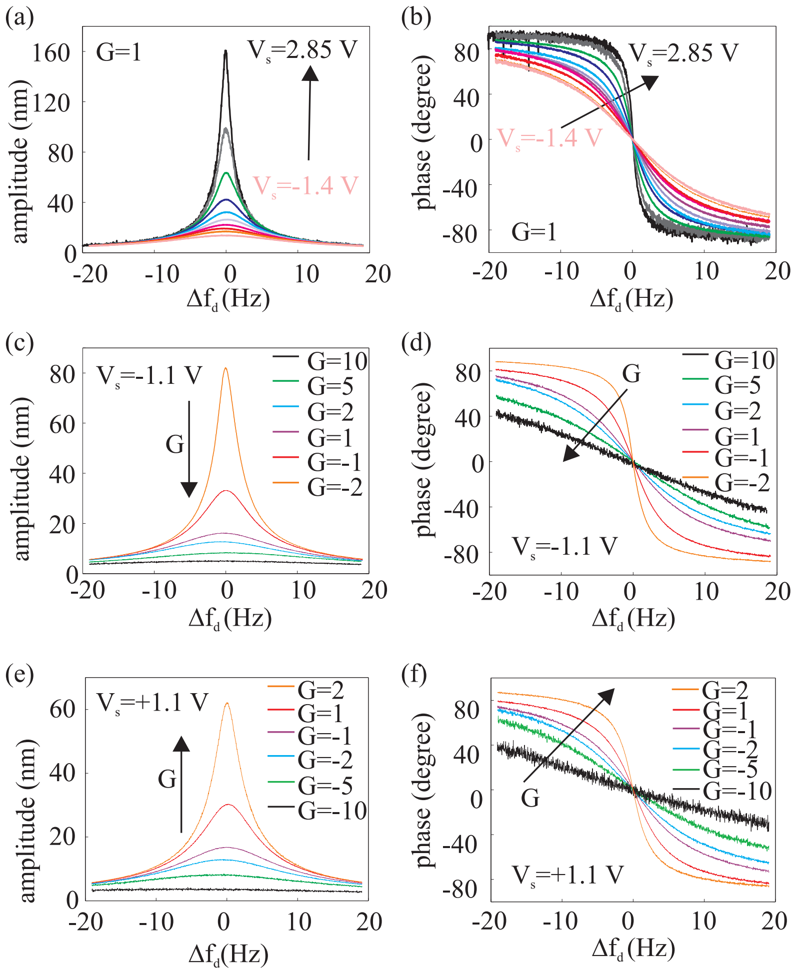

Figure 2.5: Resonance curves of cantilever A for varying $V_s$ and $G$. The left column shows the cantilever displacement amplitude vs. frequency shift of the shake piezo relative to the resonance frequency of the cantilever ($\Delta f_d \equiv f_d - f_c$). The right column shows the corresponding phase vs. $\Delta f_d$. The black arrows point towards increasing $V_s$ or $G$. (a,b) Resonance curves for gain $G = 1$ and varying $V_s$. The shake piezo drive amplitude for the two traces with the highest $V_s$ (gray and black curves) is a factor of 5 smaller than for the other curves to avoid damaging the cantilever from large oscillation amplitudes. The oscillation amplitude shown in the plot is scaled accordingly for better comparison, leading to the artificial appearance of a larger noise level. (c,d) Resonance curves for $V_s = -1.1\,\text{V}$ and varying $G$. (e,f) Resonance curves for $V_s = +1.1\,\text{V}$ and varying $G$.

two standard deviations of the measured model input parameters. There are no free parameters in the model. Most importantly, the model confirms that the non-linear term does not adversely affect our ability to set the value of $Q$.

One environment in which $Q$ control may be particularly useful is in high vacuum, where the reduction in air friction damping increases $Q$, which in turn leads to a larger time constant $\tau$. The scan speed is limited by the minimum dwell time $\tau$ required for the cantilever to adjust to the local environment at each pixel.

In Figure 2.7, we demonstrate the ability to increase scan speed by reducing $Q$. The data is collected by scanning at a constant height over a $VO_2$ sample surface while recording the frequency shift. Each image is recorded under identical conditions, including scan height, scan speed, sample bias, and oscillation amplitude. The only difference is that $Q = 13,000$ in (a), while in (b) we have reduced $Q$ to 5,900. In the reduced-$Q$ case, the transient response time of the cantilever is shortened, allowing faster response of the frequency shift to the local environment. For native $Q$, the slower response time of the cantilever smears the features of the surface. We have also verified that images recorded at the two values of $Q$ become nearly identical if the scan speed is reduced to allow full dwell time $\tau$ at each pixel.

In summary, we demonstrate a reliable method to reversibly control $Q$ *in situ* via capacitive coupling of the cantilever to the environment. Modeling the behavior of the cantilever, we explain the dependence of $Q$ on the tunable parameters $G$ and $V_s$. The method can be implemented in any system with a conductive cantilever and a conductive sample (or sample mounted on a conductive holder). We can tune $Q$ over a typical range of approximately two orders of magnitude. We confirm that this

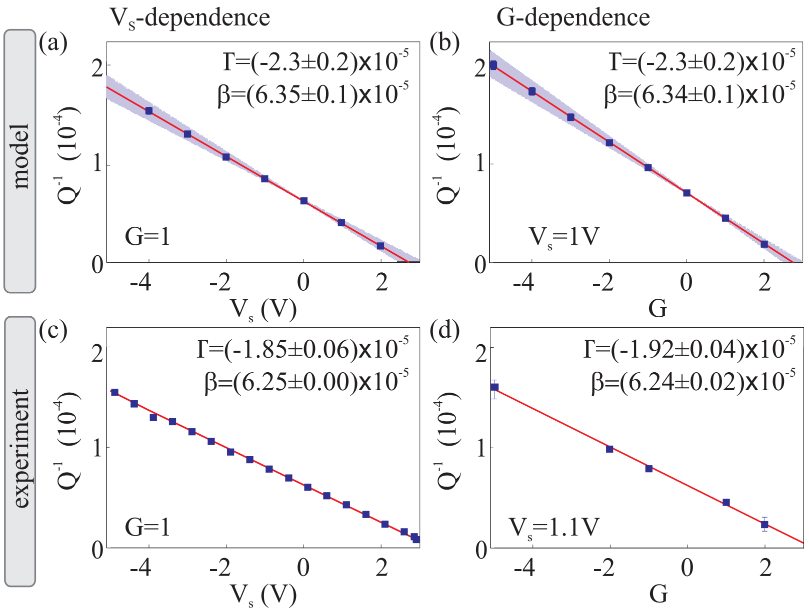

Figure 2.6: Comparison of our model (top) to experimental data recorded with cantilever A (bottom). The left column shows $Q^{-1}$ vs. $V_s$ for fixed $G = 1$; the right column shows $Q^{-1}$ vs. $G$ for fixed $V_s = 1\,\mathrm{V}$ and $V_s = 1.1\,\mathrm{V}$ for model and experiment respectively. (a,b) The individual values for which $Q$ was modeled are shown as blue squares. The shaded area shows the range of slopes ($\Gamma$ values) corresponding to the statistical uncertainties in the model input parameters. (c) Each blue square represents the average of $Q^{-1}$ recorded at four different lateral positions of the tip above the sample; each error bar represents the standard deviation of those four measurements. (d) Each blue square represents a single measurement of $Q^{-1}$. We recorded analogous $G$-dependent datasets for eight different $V_s$ values, from which we derived an average $Q^{-1}$ value for each $G$, after dividing out the known $V_s$-dependence. The error bars show the difference between the depicted $V_s = 1.1\,\mathrm{V}$ dataset and the average value from all eight datasets. In all panels, linear fits to the modeled or measured data are shown in red, and the fitting parameters $\Gamma$ in $\mathrm{V}^{-1}$ and unitless $\beta$ as defined in Eq. (2.3) are given. The reported errors in $\Gamma$ and $\beta$ are dominated by the statistical uncertainties in the model input parameters in (a,b), and by the standard error of the least squares fit in (c,d).

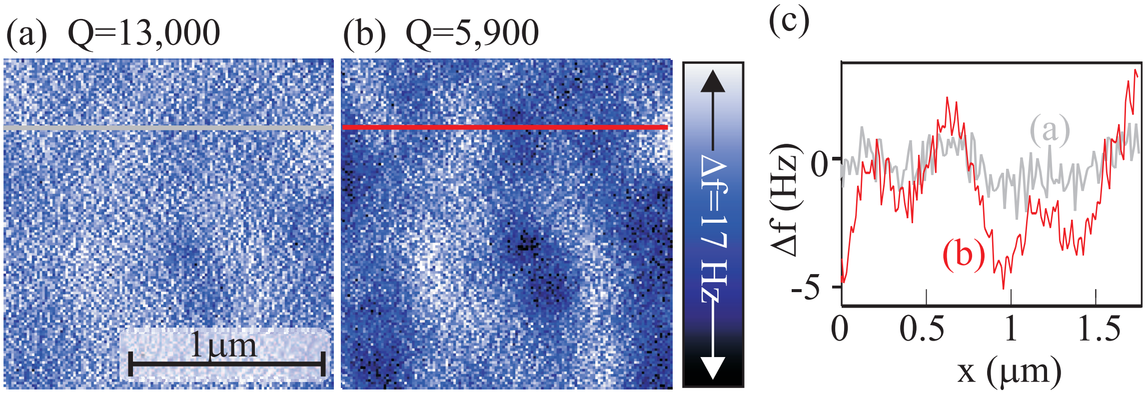

Figure 2.7: Example images at $Q_n = 13,000$ (a) and reduced $Q = 5,900$ (b) on a $VO_2$ film, acquired with cantilever B. (Note that the $Q_n = 13,000$ stated here is 5% lower than that quoted in table 2.2 because the table shows $Q_n$ for the cantilever 1 $\mu$m from the surface, whereas here we state $Q_n$ at imaging height 10 nm above the surface at -6 Hz setpoint.) Both images are recorded in 24 s. The red and grey traces displayed in (c) are cross sections through the data along the corresponding lines. By reducing $Q$, the resolution is increased at unchanged scan speed.

method of $Q$ reduction may be used to improve the quality of frequency shift images for fast scans.

# Chapter 3

# Mapping Local Properties of Vanadium Dioxide Thin Films

## 3.1 Introduction

Vanadium dioxide ($VO_2$) is a transition metal oxide that undergoes a first order structural and electronic phase transition near 340 K. As unstrained $VO_2$ is heated through the critical temperature, the crystal structure changes from monoclinic (M1) to rutile (R), and the conductivity increases by several orders of magnitude. Previous work suggests that the insulator-to-metal transition (IMT) may also be triggered by increasing carrier concentration or applying an electric field [46, 5, 55, 20, 57, 59].

Having been the subject of study for over half a century[30], $VO_2$ remains relevant for both fundamental and technological reasons. On the fundamental physics side, $VO_2$ has attracted attention as a strongly correlated material[40], in which the nature of the IMT remains controversial. Some authors have claimed the IMT in $VO_2$ is a rare example of a Mott transition near room temperature[39], while more recent work explains the insulating phase through a hybrid Peierls-Mott mechanism[52]. From a practical standpoint, the IMT enables a wide variety of applications for $VO_2$. Thin films are the most promising for most applications, as single crystals degrade with repeated cycling through the transition[27, 3]. However, different applications require different optimization of film properties. For example, both sensors[25] and memory[42] are promising applications, but for sensors, a small transition hysteresis is ideal, while memory applications require the opposite. Due to the variety of physical properties called for by different applications, there has been much interest in tailoring $VO_2$ film growth parameters to alter the characteristics of the transition[31].

The properties of $VO_2$ thin films depend strongly on the substrate, oxygen stoichiometry, transition metal doping, and grain structure[33]. In this context, the ability to locally characterize the structural and electronic properties of $VO_2$ thin films may play an important role in guiding their development. Here, we present a conducting atomic force microscope (CAFM) data acquisition scheme to obtain simultaneous topographic and electronic information. By applying a bias voltage to the sample with respect to tip, we trigger the IMT and record current-voltage ($I-V$) curves at each pixel in a scan frame. The resultant dataset gives a comprehensive picture of the properties of the $VO_2$ thin film. We present maps of several properties, including the transition voltage, a count of the number of transitions observed with increasing sample bias, and evaluation of the Poole-Frenkel conductance regime leading up to the transition.

## 3.2 Experimental Methods

We study a polycrystalline film of $VO_2$, of thickness 150±25 nm, grown by RF sputtering onto a highly As-doped Si substrate. To study the film, we use a home built AFM with a conductive cantilever in contact mode. We use an interferometer to measure the deflection of the cantilever as it makes contact with the surface. A feedback loop holds the interferometer signal constant, allowing us to maintain consistent contact force between the cantilever and sample. We gather local electronic information in a 500 nm x 500 nm region of the surface by sweeping the sample bias four times at each location in a grid on the sample. The results of the four sweeps are consistent with each other, ruling out sudden changes in contact resistance or film quality. All data presented here were obtained from the second sweep. During each sweep, we cycle the sample bias from 0 to 15 V and back, measuring the current at 50 mV intervals. Topographic information from the interferometer (figure 1a) is continuously recorded at each point. This technique should be distinguished from previous work, which presented individual $I-V$ curves at a single location of the sample[55, 19] or current maps acquired by scanning across the sample with a constant bias voltage[19]. Figure 3.1 illustrates the data acquired using the new procedure. $I-V$ sweeps similar to those in Figure 3.1(b) are taken at every location in the scan frame. These curves are each similar to the individual curves reported previously[19]. Collecting multiple $I-V$ curves at every location in the scan frame allows us to verify repeatability, and to extract local electronic properties of the sample and study them in the context of the simultaneously acquired topographic data.

At low sample bias, the $VO_2$ is in an insulating state. As the bias is increased, we see a sharp jump in current and a subsequent linear relationship between the current and the bias, indicating the transition to the metallic state. (The large current transient is due to stray capacitance in this system.) The transitions are likely induced by Joule heating[19]. As the current reaches a critical value, the film locally reaches the transition temperature. The subsequent jump in current provides further heating, feeding back positively on the transition. Figure 3.1(c) shows the measured current at 2 V bias, illustrating the grain-dependence of the current. Individual grains can be clearly resolved in the current map; the boundaries between these grains are even more pronounced than in the corresponding topography. These boundaries are used to create the grain overlay shown in red, which is superimposed on all images.

In the metallic regime, the slope of the $I-V$ curve at each location on the sample gives the local resistance through the film. We present a map of this measured resistance in Figure 3.2(a). We compare the measured resistance to a conservatively estimated upper bound on the resistance across a single grain: using resistivity $\rho \approx$ 0.001 Ω-cm[21] in the metallic state, diameter 50 nm, and thickness 150 nm, we compute the resistance across the grain to be ≈1 kΩ. The measured resistances are about 15 times larger than the estimated upper bound for conduction through a single such grain, indicating that Figure 3.2(a) maps primarily the contact resistance. Accordingly, the grain boundaries in Figure 3.2(a) are less sharp than in the current map in Figure 3.1(c). There are two main features to note in this figure. First, the measured resistance appears highly erratic in the boundary regions between grains, an observation consistent with changes in the quality of contact between the tip and sample in regions of rapidly varying topography. Second, there is a gradual trend

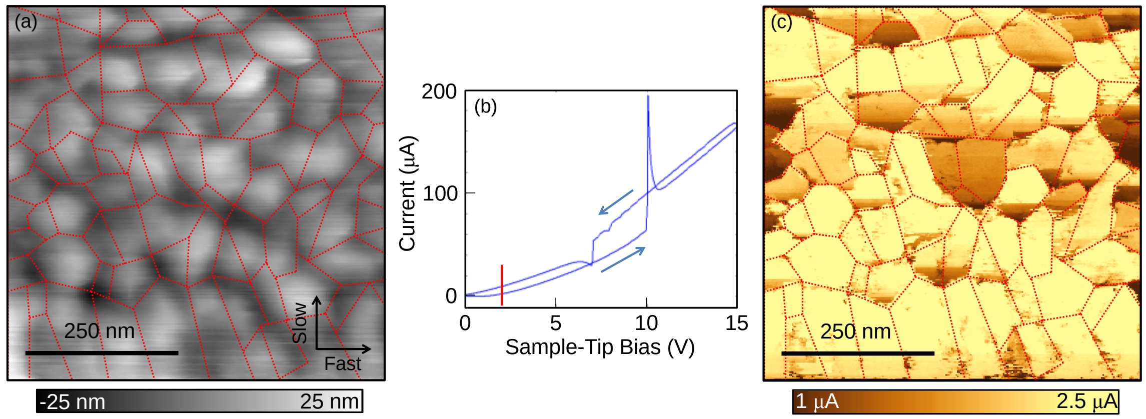

Figure 3.1: (a) Topography determined from feeding back on the interferometer signal, ensuring a constant cantilever deflection, i.e. constant tip-sample force. The fast and slow scan directions are indicated. (b) A typical I-V curve. The red bar demonstrates the voltage used to plot the current in (c), and the blue arrows show the direction of the sample bias sweep for each curve. (c) Map of the current at 2 V sample bias. This map is used to produce the grain overlay shown in red.

toward lower resistance near the top of the scan frame, which may result from changes in the tip over the course of the scan. However, the contact resistance remained constant throughout all four voltage sweeps at each single location.

## 3.3 Results and Discussion

### 3.3.1 Intermediate states

The details of the IMT in $VO_2$ remain the focus of present research. One particularly active area concerns the existence of an intermediate state between the insulating monoclinic state (M1) and the metallic rutile state (R). Early work found evidence of the intermediate monoclinic M2 insulating state in $VO_2$ under uniaxial stress[38].

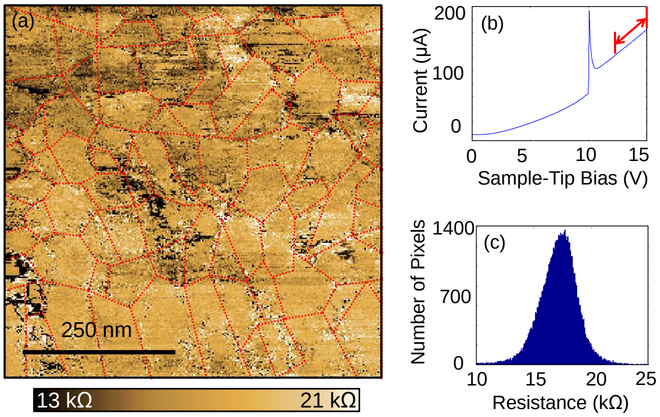

Figure 3.2: (a) Map of the local resistance through the film in the metallic state, as determined from fits to the linear region of the I-V curves. This map reflects primarily the tip-sample contact resistance. (b) The region between the red vertical bars is used to calculate the resistance. (c) Distribution of resistances throughout the field of view in (a).

Recent X-ray diffraction experiments on $VO_2$ on c-$Al_2O_3$ have shown evidence of an intermediate insulating structural state, possibly the M2 state, tied to strains in the material due to lattice mismatch with the substrate[34]. These experiments did not reveal a similar state when repeated on $VO_2$ on a Si substrate. Pump-probe experiments have provided evidence of a non-equilibrium intermediate monoclinic metallic state[18]. Other x-ray diffraction experiments have not identified intermediate structural states, but have inferred the existence of an intermediate metallic state similar to that reported by Kim *et al.*[32]. Simultaneous scanning near-field infrared microscopy (SNIM) and nanoscale X-ray diffraction experiments have further complicated the picture. Qazilbash *et al.* showed a monotonic electronic transition with increasing temperature, but non-monotonic structural transitions, which they hypothesize may be due to decoupling of the electronic and structural transitions in a narrow range of temperatures[41]. Other SNIM work has shown the co-existence of metallic and insulating phases within a single grain of $VO_2$[10]. The existence and nature of intermediate structural and electronic states in $VO_2$ is not yet resolved.

While our experiment cannot directly probe the structural state of the $VO_2$ thin films, we have identified behavior in the local $I - V$ curves that may be consistent with intermediate states. Within many of the sweeps, we identified two transitions. These transitions manifest as discrete jumps in the conductance. When we observe two transitions in a single curve, the first transition is always smaller and the sample remains in an insulating state until the second, larger transition. We ascribe the subsequent large transition occurring at higher voltage to the IMT, as it leads to a linear $I - V$ relationship.

Figure 3.3(a) shows a map of the number of transitions identified at each location on the sample. Most grains display only a single transition. However, some grains display two transitions across the entire grain, as exemplified in the blue- and yellow-outlined grains in Figures 3.3(a) and (b). Figure 3.3(c) illustrates a typical sweep displaying two transitions. This behavior may be consistent with previous work showing intermediate structural states tied to strain in the film[34] or other non-equilibrium intermediate states. While strain has not been shown to induce a macroscopically stable M2 phase in $VO_2$ on Si, as is the case for an $Al_2O_3$ substrate, there may be local strains that lead to conditions favorable for the M2 state. We cannot rule out that these features are due to microstructural factors, such as transitions triggered in underlying grains. However, due to the high correlation with boundaries of surface grains, we suspect that these transitions are a property of the

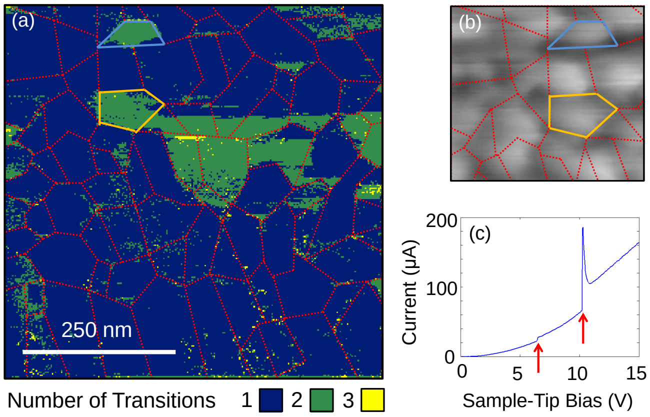

Figure 3.3: (a) Map of the number of transitions counted from the $I - V$ sweeps at each location on the sample. (b) Cropped region of the topography at the same scale as in (a). (c) The red arrows show the locations of the transitions in a sweep containing two. Grains containing two transitions throughout are outlined in blue and orange in both (a) and (b).

grains themselves. If the initial transition indicates a transition to the M2 state, then we have evidence that the M2 phase in pure $VO_2$ has a higher conductivity than the M1 phase. We also note that we do rarely detect up to three transitions near the boundaries of grains displaying two transitions. This may result from the observation of the intermediate transition in neighboring grains when the tip makes contact with both simultaneously.

### 3.3.2 Electronically triggered transition

Another ongoing debate surrounding the IMT in $VO_2$ is whether the transition can be triggered purely by the application of an electric field, as opposed to the effects of Joule heating. A variety of experiments have provided conflicting results. In 2002, Boriskov *et al.* found they could alter the transition temperature by applying a field in the range of $10^5$ to $10^6$ V/cm[5]. In addition, they found that the high-field switching was not consistent with enhanced carrier density alone. From magnetotransport studies, other researchers have concluded that the increase in Hall carrier density does indeed account for the change in resistivity across the IMT[46]. Later experiments have supported the electric field-induced view of the transition[55, 20, 57, 59]. In addition, results from simulations have shown that the effects of Joule heating may not be large enough to trigger the IMT in $VO_2$, but that they may be sufficient to trigger a structural transition after the transition to the metallic state[11]. CAFM experiments have supported the view that Joule heating plays an important role. Early contact-mode bias sweeps suggested that the IMT could be understood as a competition between Joule heating and heat dissipation[19]. Subsequent CAFM studies argued that there is indeed an electric-field triggered transition, but that the sample oscillates between the two states when in tunneling mode[55]. In contact mode, the sample exhibits a sharp IMT, indicating that the current reinforces the transition to the metallic state. Ultrafast spectroscopy experiments further complicate the picture, as researchers have found that the IMT lags the structural transition, and the electronic transition is ultimately structurally driven[7].

In Figure 3.4, we present a map of the IMT voltage $V_T$, as determined from the sample bias applied at the instant of abrupt current increase. These results confirm and extend those of previous CAFM studies. For example, the field across our sample during the IMT is typically around 3-4 $\times$ $10^5$ V/cm, consistent with reports of electric field-driven electronic phase transitions in $VO_2$[5, 55, 20, 57, 59]. However, observations in previous CAFM measurements do suggest that Joule heating

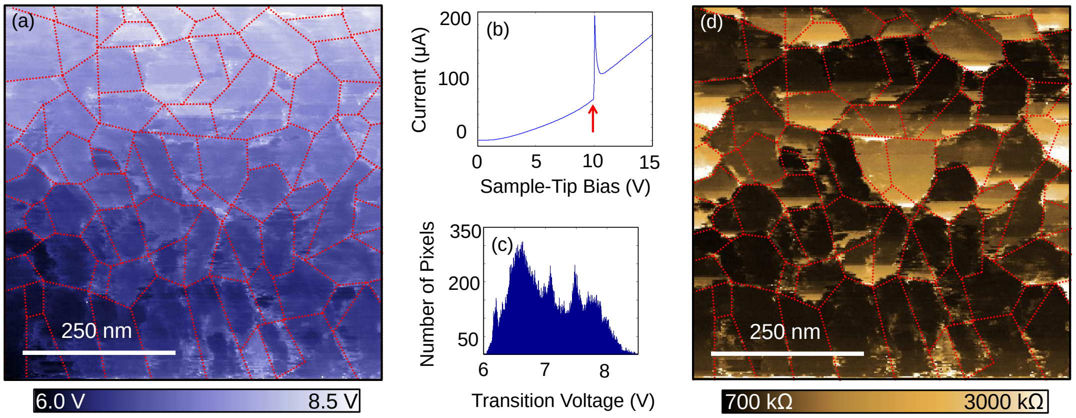

Figure 3.4: (a) Map of sample bias at transition $V_T$, extracted from the $I-V$ curves. The boundaries of the grains display a larger transition voltage, consistent with the larger measured resistance through the sample at these locations.(b) A typical $I-V$ trace with an arrow denoting the sample bias at transition. (c) The distribution of transition voltages across the sample. (d) The calculated resistance through the film at 2V after subtracting the contact resistance from figure 2(a). The regions at the grain boundaries have larger resistance.

reinforces the transition, as increases in current further heat the sample above the transition temperature[55, 19]. In our work, we observe larger transition voltages at the grain edges (Figure 3.4(a)). These grain edges tend to display a larger resistance in the insulating regime (Figure 3.4(d)), resulting in a lower current. The larger resistance at these boundaries, which may be due to local variations in strain or stoichiometry, leads us to believe that current and thus Joule heating is important in triggering the transition. The transition voltage map further shows that each individual grain has a consistent final transition voltage across the grain. That is, there is very little variation within each grain.

### 3.3.3 Local Poole-Frenkel Conduction

We can also use the individual $I-V$ curves to obtain information about other local properties of the sample. In the insulating state, the Poole-Frenkel (PF) effect may be a dominant conduction mechanism over an intermediate voltage range preceding the IMT. Transport measurements on $VO_2$ thin films have shown this to be the case for both in-plane and transverse conduction[20, 57, 56, 58]. However, there have been few reports in which this effect is used to quantify the properties of $VO_2$ films.

Poole-Frenkel conduction results from thermal excitation of electrons to the conduction band in the presence of a strong electric field. The current induced by the field satisfies[48]

$$\ln\left(\frac{I}{V\sigma_0}\right) = \frac{e}{k_B T}\left(\frac{e}{\pi \epsilon d}\right)^{1/2} V^{1/2} + C \tag{3.1}$$

Where $C$ is a constant proportional to the logarithm of the low-field conductivity, $\sigma_0$. From this expression, we see that the slope of $\ln(I/V)$ versus $V^{1/2}$ depends only on fundamental constants and the sample thickness $d$, temperature $T$, and permittivity $\epsilon$.

In Figure 3.5(a), we show an $I-V$ curve plotted so that a PF expression would fall on straight line. We see that there is a region from ≈4 V to 1 V prior to $V_T$ over which PF conduction appears dominant. We can fit straight lines to these regions, from which we create a PF fit coefficient map [Figure 3.4(c)]. This map is similar to previous maps in that boundaries of the grains are clearly visible. The median value of the fit coefficient across the map is 0.039 $\mathrm{mV}^{-1/2}$. Using the nominal film thickness of $d \approx 150$ nm, this value corresponds to parameters of $\epsilon \approx 38$, $T \approx 300$ K. From previous capacitance measurements, the permittivity of $VO_2$ is $\approx 36$ at room

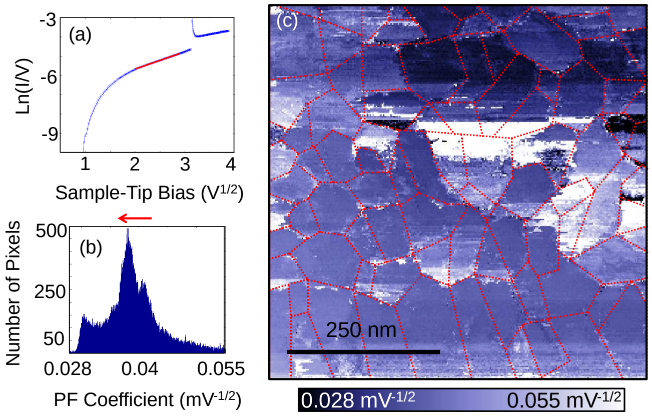

Figure 3.5: (a) Plot of $\ln(I/V)$ versus $V^{1/2}$, showing the linear regime over which PF conductivity dominates. The red line is a fit to the linear region, and the slope provides an estimate for the dielectric constant. (b) A histogram of the slope values. The red arrow indicates the direction of increasing T and epsilon. (c) A map of the PF fit coefficient.

temperature and increases by several orders of magnitude as the temperature increases through the transition[58]. From the distribution of values in Figure 3.4(b), we see that the fit coefficient can be as small as 0.03 $\mathrm{mV}^{-1/2}$, corresponding to a temperature of approximately 315 K [Figure 3.6(a)]. By reducing the fit length and fitting a succession of regions in the PF regime, we observe a downturn in the slope with increasing sample bias, which is evidence of increasing permittivity and temperature with increasing sample bias before breakdown of PF conduction about 1 V prior to $V_T$. While there are significant uncertainties arising from the film thickness, this method enables the local measurement of both the permittivity and temperature of the sample to the extent that $\epsilon(T)$ is known.

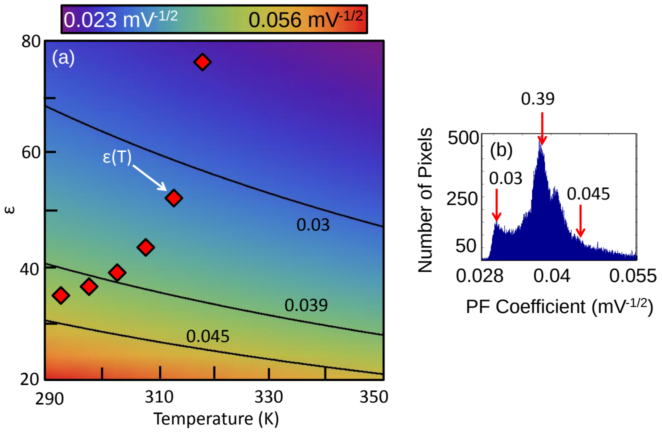

Figure 3.6: (a) A contour plot of the PF coefficient as a function of permittivity and temperature, assuming a sample thickness of 150 nm. The black circles labeled $\epsilon(T)$ show data on the permittivity of $VO_2$ as a function of temperature taken from Yang *et al.*[58]. In (b), red arrows identify the values used for the contour lines in (a).

## 3.4 Summary

We used CAFM to probe the local properties of a $VO_2$ thin film. We resolved individual grains both in current maps and in maps of local properties. We observed individual grains that demonstrate multiple jumps in current as we increased the sample bias, which may be consistent with intermediate states. PF fits in the insulating regime are consistent with slight sample heating in the insulating phase. More broadly, we have demonstrated the ability to use CAFM to probe local properties of $VO_2$ thin films in relation to their structure. As the range of potential applications of this material expands, this technique may prove useful in the characterization of $VO_2$ thin films produced under different conditions. Future experiments may improve on this technique by reducing the contact force between the cantilever and the sample while changing the lateral position, as this motion likely leads to systematic changes in the tip of the cantilever.

# Chapter 4

# MFM Studies on $Nd_2Fe_{14}B$

## 4.1 Introduction

$Nd_2Fe_{14}B$ is a strong rare-earth ferromagnetic compound commonly used in industrial applications. Below the Curie temperature of 565 K, the moments of the Nd and Fe atoms align ferromagnetically [14]. The crystal has tetragonal lattice symmetry, and the easy magnetic axis is aligned with the crystallographic c-axis between room temperature and the Curie temperature. Figure 4.1 shows the crystal structure of the material [14]. Below $T_{SR} = 135$ K, $Nd_2Fe_{14}B$ undergoes a second-order transition in which the the magnetic easy axis rotates away from the c-axis [14, 37]. There are four symmetry-equivalent directions into which the moments may align, reaching a maximum angle of 28° from the c-axis well below the transition [24]. There have been a large range of studies exploring the magnetic domain structure in $Nd_2Fe_{14}B$. For example, early work used the Bitter technique to observe the magnetic domains in large grains of $Nd_2Fe_{14}B$ [8]. Other researchers have explored the domain structure

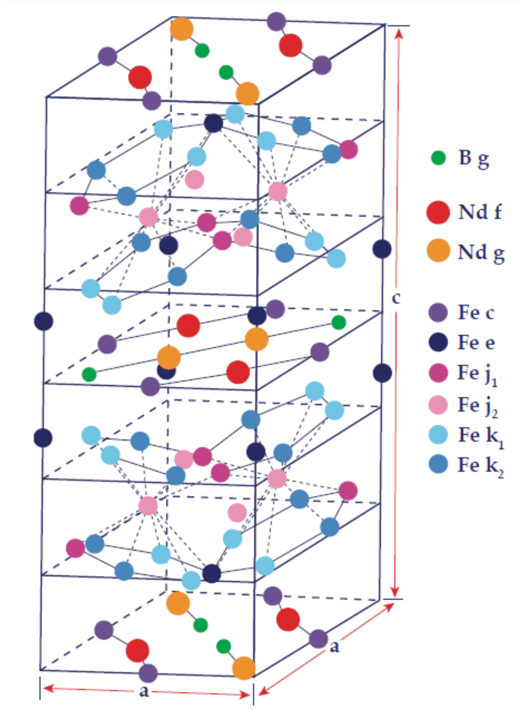

Figure 4.1: Crystal structure of $Nd_2Fe_{14}B$. The crystallographically distinct lattice sites are labeled. This figure is from reference [15].

using the magneto-optic Kerr effect (MOKE) [36, 24] or magnetic force microscopy [1, 50]. In Figure 4.2, we present MOKE images from reference [36], which illustrate the evolution of magnetic domain structure through the spin reorientation transition.

In the work presented here, we imaged the surface of $Nd_2Fe_{14}B$ both in contact mode and non-contact mode. In non-contact mode, we imaged using cantilevers with both magnetic and non-magnetic tips. When scanning the surface using a non-magnetic tip, we found the surface to be flat. Using a magnetic tip, we observe a great deal of structure, which we interpret to be magnetic in origin. We present images of the the sample surface at room temperature and at a variety of temperatures around

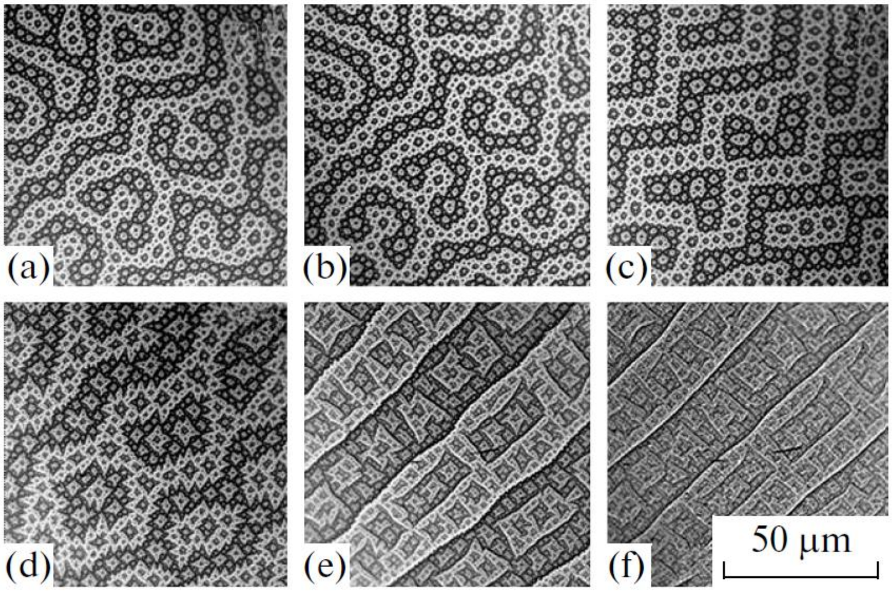

Figure 4.2: MOKE images of the surface of $Nd_2Fe_{14}B$ perpendicular to the c-axis. The images were taken at (a) 285 K, (b)200 K, (c) 165 K, (d) 118 K, (e) 113 K, (f) 20 K. This figure is from reference [36]

the spin reorientation transition. In addition, we present contact mode scans taken with a magnetic cantilever, further confirming the flat topography of the sample.

## 4.2 Experimental Methods

Our sample consists of a large single crystal of $Nd_2Fe_{14}B$. Figure 4.3 shows an optical image of the surface of the sample surface prior to preparing the sample for imaging. To prepare the sample, we first thermally demagnetized it by heating it above the Curie temperature of 565 K. After allowing it to cool, we cleaned the sample with a sonicator in a bath of isopropyl alcohol and distilled water. We then mounted the sample on the sample stage so the surface normal to the c-axis faces the cantilever, securing it in place with conductive epoxy. Upon installation in the microscope, we made electrical connections to both the sample and cantilever.

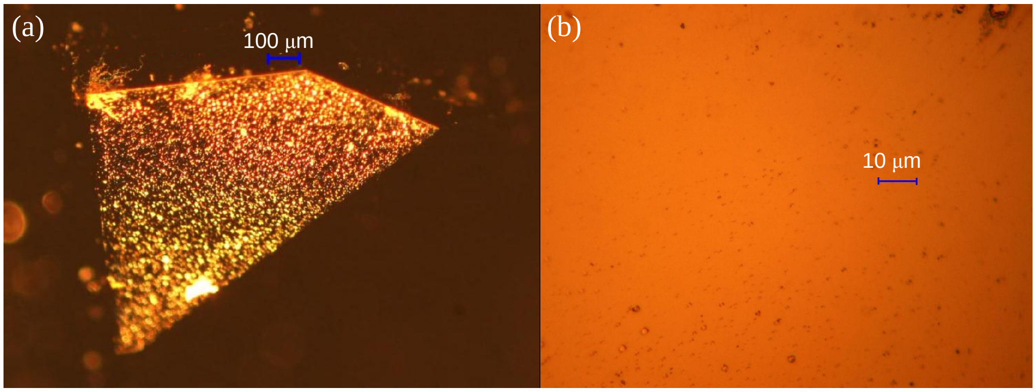

Figure 4.3: Photographs of the $Nd_2Fe_{14}B$ sample surface at 5x (a) and 100x (b) magnification.

## 4.3 Imaging without Magnetic Sensitivity

Prior to scanning with a magnetically sensitive tip, we scanned the surface with a non-magnetic cantilever to determine the surface topography. We could then compare the topography to the structure observed with tips sensitive to the stray magnetic field from the sample.

Figure 4.4 shows an image of the sample surface taken at room temperature in high vacuum with a nonmagnetic cantilever ($\mu$masch model NSC16). The Z-controller set point is an oscillation frequency shift of $-6$ Hz. The surface of the $Nd_2Fe_{14}B$ sample is quite dirty (as is apparent from the optical images), and feedback can become unstable over certain regions. For example, there are two significantly elevated regions visible in the scan, and feedback was somewhat unstable over these regions. However, the significance of this scan can be seen in the other regions of the scan frame. We observe that the surface of the sample is quite flat, with height variations on the order of tens of nanometers over the 3 $\mu$m by 3 $\mu$m scan frame.

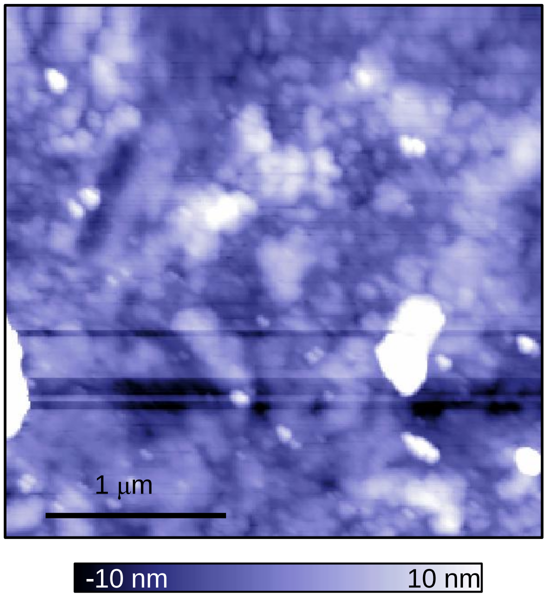

Figure 4.4: Topographic image taken with a non-magnetic cantilever in non-contact mode. The frequency shift signal serves as the input to the Z-controller, which is active.

We can also obtain topographic information by scanning in contact mode. Figure 4.5 shows a 59 $\mu$m by 59 $\mu$m topographic scan in contact mode near 82 K using a tip with a ferromagnetic coating. We obtained this image using a cantilever with a magnetic tip after acquiring images with magnetic sensitivity (Figure 4.8). From this topography, we see again that the surface of the sample is quite flat. There appears to be little structure in the surface aside from bright splotches most likely corresponding to surface contamination. As we will see in the next section, scans taken in non-contact mode with tips sensitive to magnetic fields reveal very different structure.

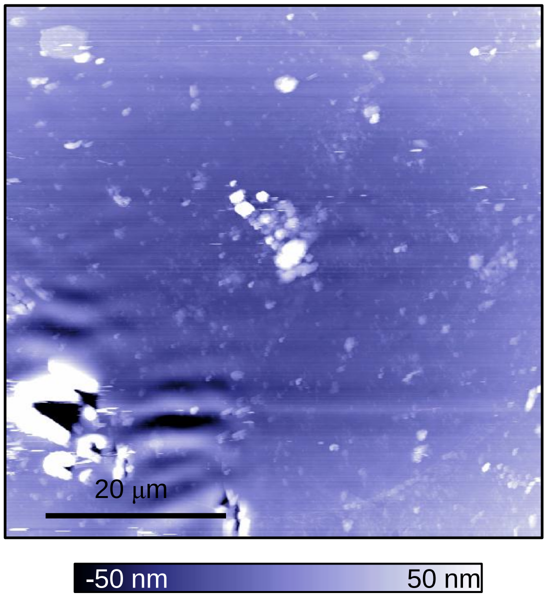

Figure 4.5: Topographic image taken with a magnetic cantilever in contact mode. The image was taken after the scans shown in Figure 4.8 and is over the same region of the sample.

## 4.4 Imaging with Magnetic Sensitivity

To acquire images with magnetic sensitivity, we must use a cantilever with a tip coated in a magnetic material. In this work, we use a Team Nanotec model HR-MFM75-ML1-5 cantilever. The cantilever is coated with a thin film of a proprietary cobalt alloy. The tip radius is less than 25 nm, and the cantilever has a resonance frequency around 75 kHz. We magnetize the tip by holding the center of a strong permanent magnet approximately one millimeter above the cantilever for about 30 seconds at room temperature. This magnetizes the tip in the direction normal to the sample surface.

We can approximate the interaction between the cantilever and sample by treating the tip as a magnetic dipole that interacts with the stray field of the sample. In this approximation, the force on the tip is given by

$$\vec{F}_{TS} = \nabla\left(\vec{m}\cdot\vec{B}\right) \tag{4.1}$$

where $\vec{m}$ is the magnetic dipole moment of the tip, and $\vec{B}$ is the stray magnetic field from the sample. The cantilever is sensitive to the component of the force parallel to the oscillation direction, which is the $\hat{z}$ direction normal to the sample surface. This component of the force is given by

$$F_{TS,z} = m_x\frac{\partial B_x}{\partial z} + m_y\frac{\partial B_y}{\partial z} + m_z\frac{\partial B_z}{\partial z} \tag{4.2}$$

Since we have magnetized the cantilever in the $\hat{z}$ direction, $m_x = m_y = 0$, and we can simplify this expression to

$$F_{TS,z} = m_z\frac{\partial B_z}{\partial z} \tag{4.3}$$

Plugging this expression for $F_{TS,z}$ into Equation 1.11, we find that the frequency shift is given by

$$\frac{\Delta\omega_r}{\omega_r} \approx -\frac{m_z}{2k}\frac{\partial^2 B_z}{\partial z^2} \tag{4.4}$$

We see that the frequency shift provides a measure of the second derivative with respect to $z$ of the $\hat{z}$ component of the stray magnetic field.

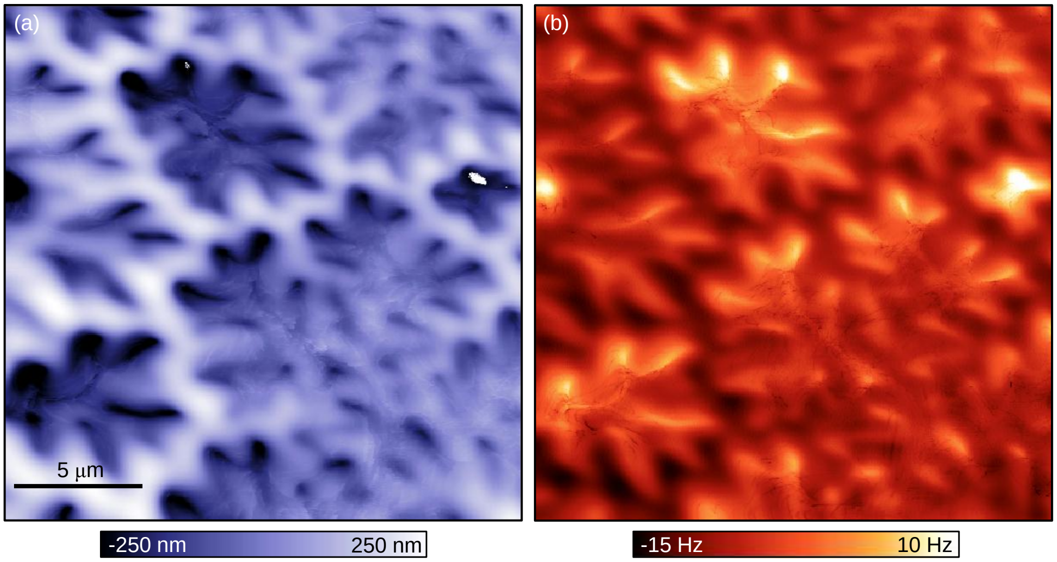

Figure 4.6: Images of the $Nd_2Fe_{14}B$ sample acquired with a cantilever with a magnetized tip. In (a), the Z-controller is active with a set point of $-60$ Hz. In (b), the Z-control is inactive and the image displays the measured frequency shift at a constant height above the surface.

Figure 4.6 presents a set of images of a 20 $\mu$m by 20 $\mu$m region of the $Nd_2Fe_{14}B$ surface taken using a cantilever with a tip magnetized normal to the sample. The images were taken at room temperature in vacuum ($1 \times 10^{-7}$) Torr). In Figure 4.6 (a), the frequency shift serves as the input to the Z-controller. The Z position in the image corresponds to a contour of constant $\frac{\partial^2 B_z}{\partial z^2}$ above the sample. Comparing this figure to the topographies in Figures 4.4 and 4.5, we see that the variations in "height" are far greater in the image with magnetic sensitivity. In addition, the shapes of the structures in the magnetic image have little in common with those in the topographic images. As a result, we believe the interaction between the magnetic moment of the tip and the stray magnetic field from the sample dominates the other interactions in these measurements. We also note that feedback can become unstable in the dark “clover-like” regions. To circumvent this instability, we turn off the Z-controller and operate in constant-height mode for the majority of the images acquired with magnetic tips. Figure 4.6 (b) shows a constant height scan over the same region of the sample, meaning the tip actually follows a flat plane trajectory above the sample. In this panel, we report the measured frequency shift, proportional to $\frac{\partial^2 B_z}{\partial z^2}$ at each location above the sample. Note that the regions largest (negative) frequency shift in (b) correspond to the highest regions in (a), consistent with the scans being taken over the same region of the sample.

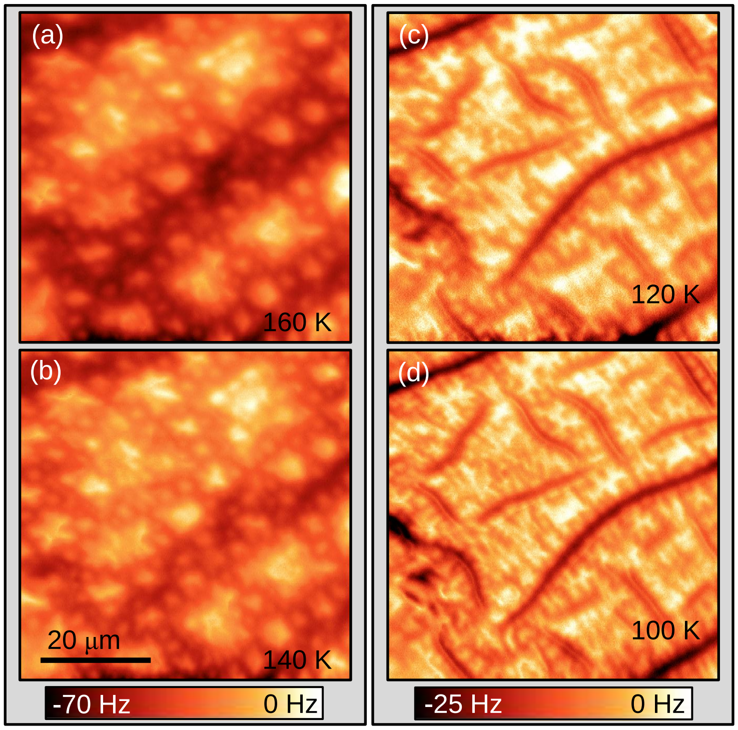

Figure 4.7: Constant height scans at (a) 160 K, (b) 140 K, (c) 120 K, and (d) 100 K. The scale bar on the left corresponds to the scans above the spin reorientation transition temperature, and the scale bar on the right corresponds to the scans below the spin reorientation temperature. Each image has been offset by a constant frequency shift so 0 Hz is the maximum value.

Figure 4.7 illustrates the temperature dependence of the magnetic structure over a broad range of temperatures around $T_{SR}$ in a 59 $\mu$m by 59 $\mu$m region of the sample. The constant height scans above $T_{SR}$ reveal magnetic structure similar to that visible in Figure 4.6, while the scans below $T_{SR}$ show a distinctly different magnetic structure, characterized by linear regions with approximately orthogonal intersections, that persists below the transition. In Figure 4.8, we investigate the temperature dependence of the transition more closely by scanning the surface at 2 K intervals from 138 K to 124 K. The topographic scan in Figure 4.5 was taken over the same region of the sample as that shown in these scans. There is no clear correlation between the sample topography and the magnetic structure we observe. This series of images shows the evolution of the magnetic structure associated with the spin reorientation transition in greater detail. We also include a scan at 90 K, well below the transition, demonstrating that the magnetic structure does not change substantially with decreasing temperature. However, we do observe that the magnetic structure continues to evolve for a range of temperatures below 135 K. We consider several potential explanations for this behavior. First, the transition may be slow, taking place over the course of hours. Second, the transition may occur over a broad temperature range. Third, the sample temperature may lag the temperature we measure. From consecutive scans at constant temperature, we have found that the magnetic structure stays constant for a particular temperature set point, which indicates that the sample temperature is stable and the transition is not slow, ruling out the first and third possibilities. As a result, we believe the transition is gradual in temperature, occurring over a range of temperatures around 135 K.

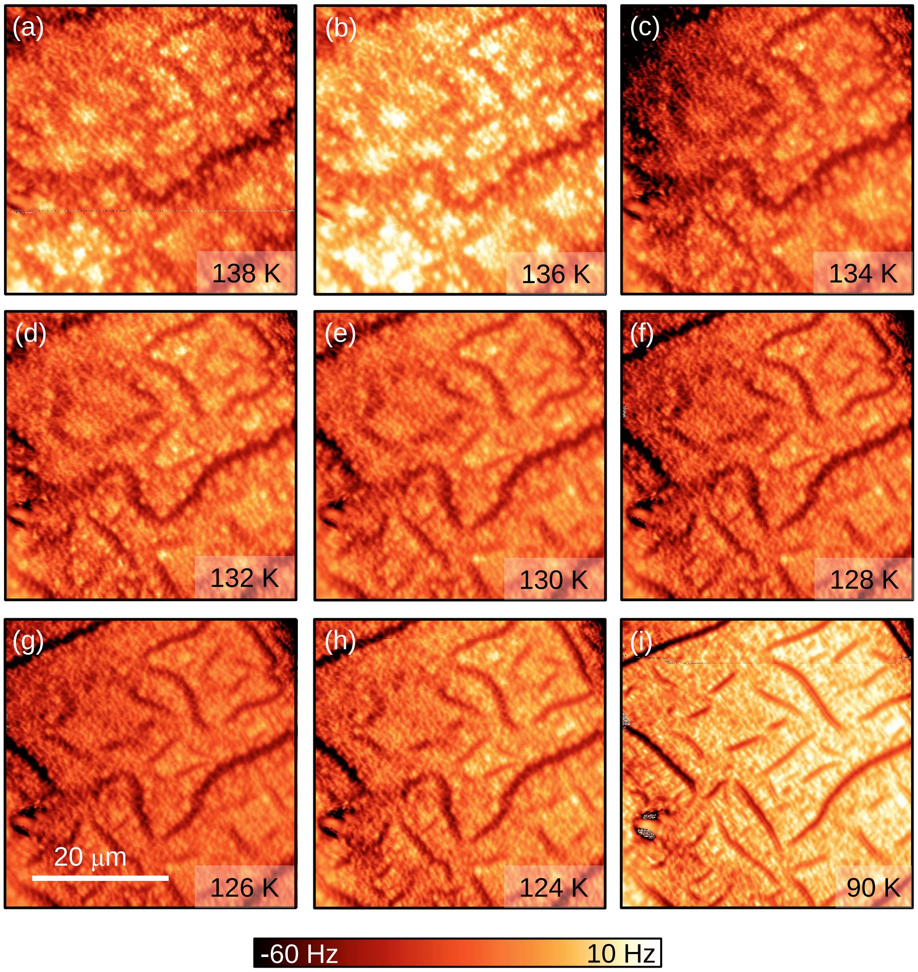

Figure 4.8: Constant height scans at (a) 138 K, (b) 136 K, (c) 134 K, (d) 132 K, (e) 130 K, (f) 128 K, (g) 126 K, (h) 124 K, and (i) 90 K. The scale bar applies to all scans in the figure. The scans were set up so the peak to peak change in frequency shift would be approximately 60 Hz. The images shown here have not been processed.

Finally, we note that we have observed small shifts in the magnetic structure of the sample at temperatures below $T_{SR}$. Figure 4.9 (a-d) shows a series of scans taken while cooling the sample from 100 K to 95. In this series of scans, there were few noticeable changes between subsequent scans. However, between Figure 4.9 (b) and (c), we noticed an abrupt change in the magnetic structure (circled in blue), that persists with continued cooling.

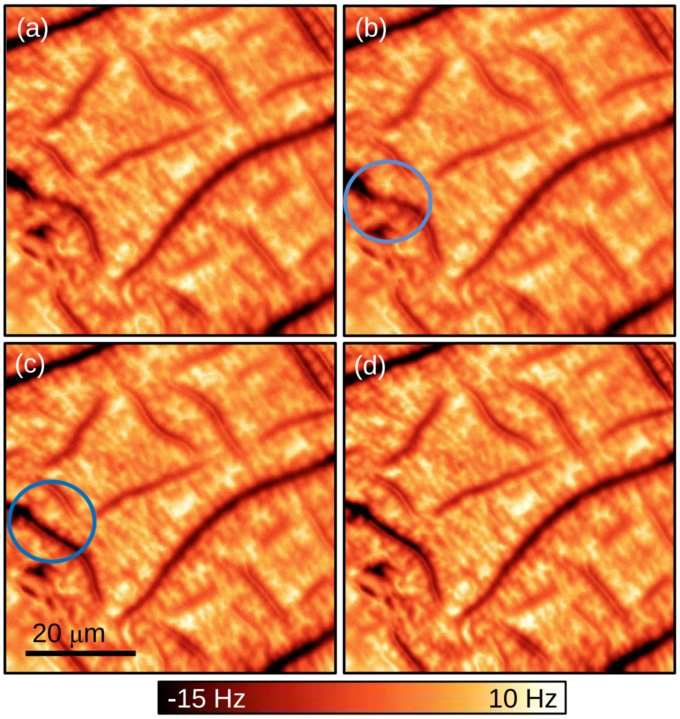

Figure 4.9: Constant height scans while cooling from 100 K to 95 K. Between images (b) and (c) there is a small shift in the magnetic structure, which is circled in blue. The change is persists to in the following scans.

## 4.5 Conclusions and Outlook

We have imaged the surface perpendicular to the c-axis of single crystal Nd$_2$Fe$_{14}$B using both magnetic and non-magnetic probes. With probes sensitive to the component of the stray magnetic field normal to the sample surface, we have resolved the magnetic structure of the sample at room temperature and near the spin reorientation transition at 135 K. We tracked the evolution of the surface magnetic structure through the transition by imaging the sample at intervals of 2 K from 138 K to 124 K. We found that this structure does not appear correlated with the sample topography. In addition, we found that the spin reorientation transition takes place gradually over a range of temperatures below 135 K. For a given temperature the magnetic structure typically appears stable in time.

One area warranting further investigation is the formation of the low temperature magnetic domain structure. Having cycled the temperature of the sample through the transition several times, we observed that the low temperature magnetic structure tends to settle into a preferred pattern. To investigate this behavior further, we could explore how the magnetic structure below the transition depends on the rate at which the sample was cooled. We could also explore the relationship between the domain structures above and below the transition temperature to determine the degree to which they are correlated.

# Appendix A

# Manual for operating the force microscope

## A.1 System overview

### A.1.1 List of components

Photographs of the front and back of the microscope with labeled components appear in figure A.1. For a schematic overview of the main components in the system, see figure A.2.

- **Cantilever head:** The top half of the force microscope. This component contains the fiber system, cantilever, shake piezo, and fiber walker.
- **Sample head:** The bottom half of the force microscope. This component contains the sample, scan piezo, and X, Y, and Z walking systems.

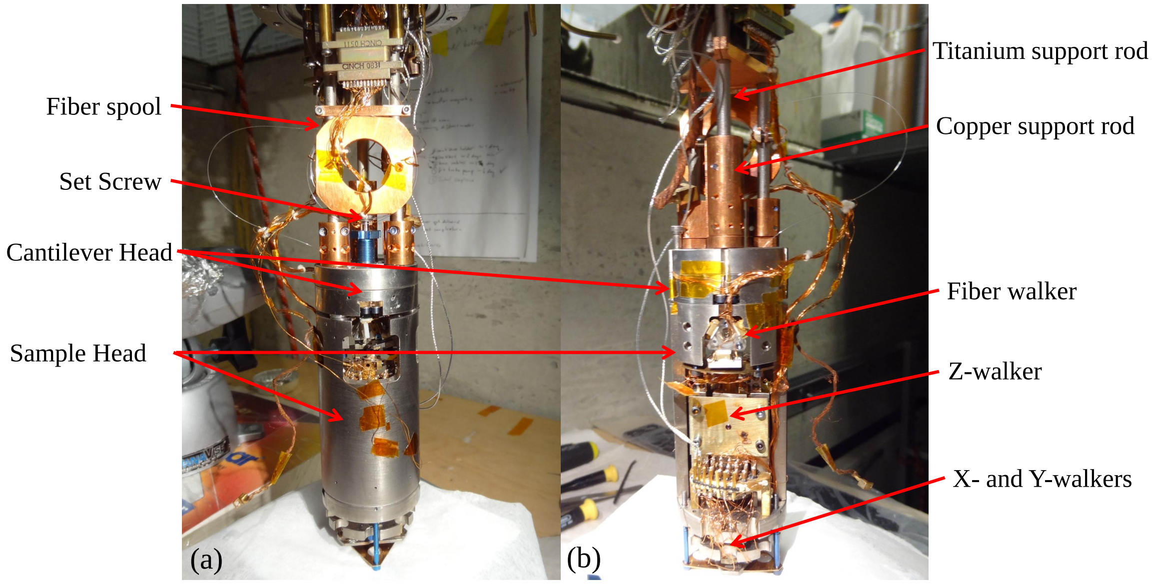

Figure A.1: Photographs of the front (a) and back (b) of the microscope.

- **W-piezo:** Commercial piezo controlling the separation between the cantilever and the fiber by translating the position of the fiber

- **Shake piezo:** Piezo stack that oscillates the cantilever. It is located beneath the cantilever holder.

- **Cantilever holder:** Steel part that holds the cantilever. The cantilever spring plate attaches to this part with two screws and secures the cantilever in place.

- **Fiber walker:** Walker that translates the cantilever relative to the fiber. Despite the name, this system translates the cantilever.

- **X and Y walkers:** Walker system that translates the sample horizontally. This system has been seldom used, but appears to be working. The walker pads are located at the bottom of the sample head.

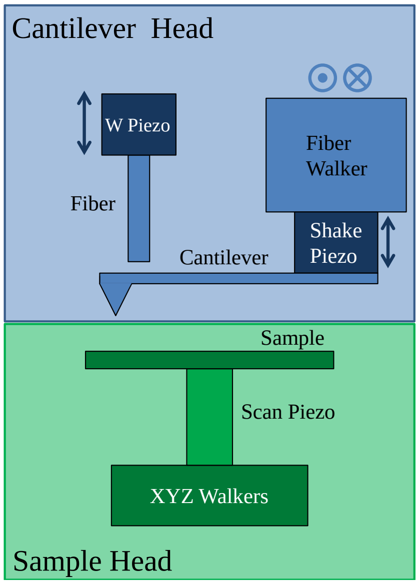

Figure A.2: Schematic overview of the main components of the microscope. The components are not to scale. The colored arrows indicate the direction of motion for the corresponding component. The fiber walker walks the cantilever normal to the page. The naming convention dates to a previous mode of operation when the optical fiber was rigidly attached to the fiber walker.

- **Z walker:** Walker system that translates the sample vertically
- **Set screw:** Screw meant to adjust the position of the fiber. Originally intended for coarse adjustment of the separation between the fiber and the cantilever, this component behaves erratically. Adjusting the screw translates the fiber both vertically and horizontally (parallel to the length of the cantilever). Adjusting the set screw is occasionally useful, as it allows alignment along the cantilever axis. However, this alignment can be achieved by other means, and it is generally wise to not touch the set screw.
- **Fiber spool:** Spool storing fiber optic cable
- **Copper support rods:** Copper rods used for thermal connections and to

support the microscope by clamping to the titanium rods

- **Titanium support rods:** Titanium rods used to support the microscope while imaging

- **Optical attenuator:** Optical component in series with the reference line. Use the screw on this device to adjust the attenuation of the reference beam. This adjustment is most-often used to center the interferometer signal at 0 V.

- **Experiment dewar:** Dewar used to keep the experimental apparatus at cryogenic temperatures. The dewar attaches to the bottom of the aluminum plate on the experimental table (figure A.3).

- **Breakout box:** Electrical breakout box attached to a vacuum feedthrough. The connections for all the walkers, the scan tube, the W piezo, the sample bias, and the thermometer and heater enter the vacuum system through this box.

- **Janis flow cryostat:** Vacuum insert into the experimental dewar (figure A.4. This component houses the microscope. At the time of this writing, the helium flow feature cannot be used due to a leak between the helium flow space and the main vacuum space containing the microscope.

- **Control electronics:** The electronics boxes in the control room used to operate the force microscope. A photograph identifying the important components appears in figure A.5.

- **Walker box:** The custom electronics box used to control the X, Y, Z, and fiber walkers.

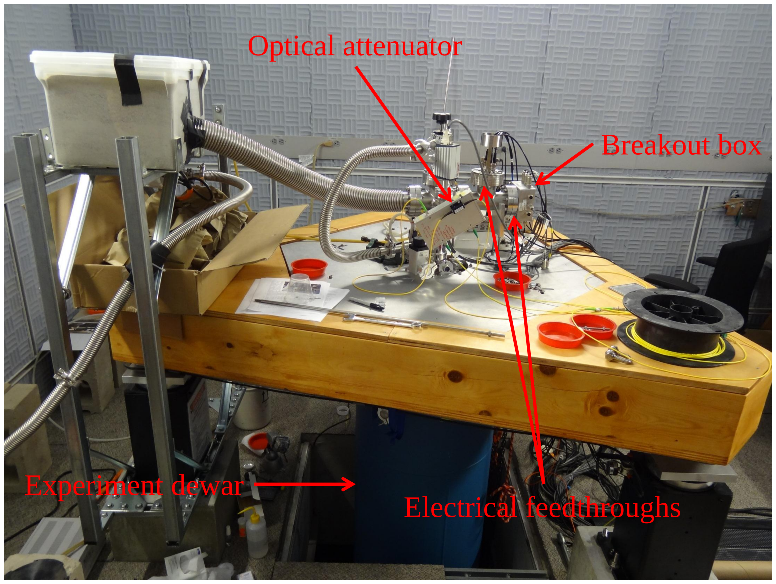

Figure A.3: Photograph of the system with the experiment dewar raised.

## A.1.2 Putting the microscope into "safe mode"

It is often necessary to put the microscope into a safe mode to prevent damaging the cantilever, fiber, sample, or other system components. For example, this is the case when attaching the vacuum can or assembling the microscope. When "safe mode" is referenced below, take the following steps:

- Withdraw the cantilever.
- Ensure that there is sufficient separation between the cantilever and the sample. At room temperature, this usually entails walking back by approximately 5000

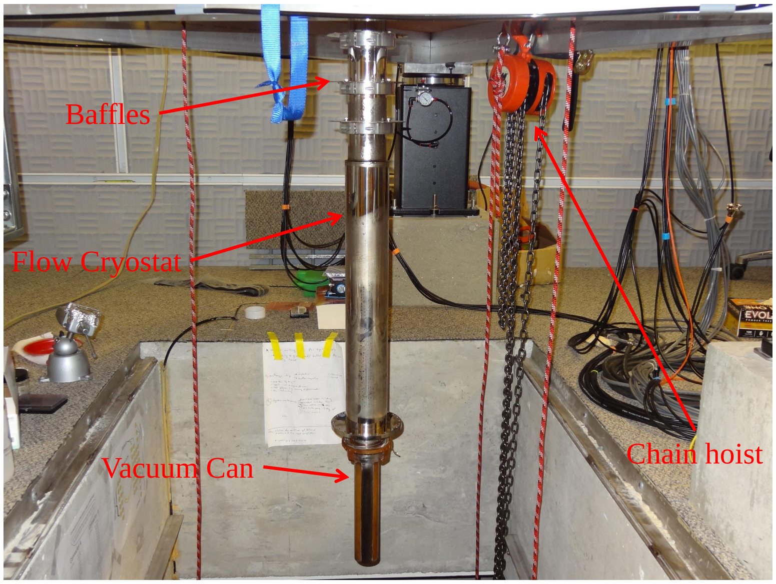

Figure A.4: Photograph of the cryostat.

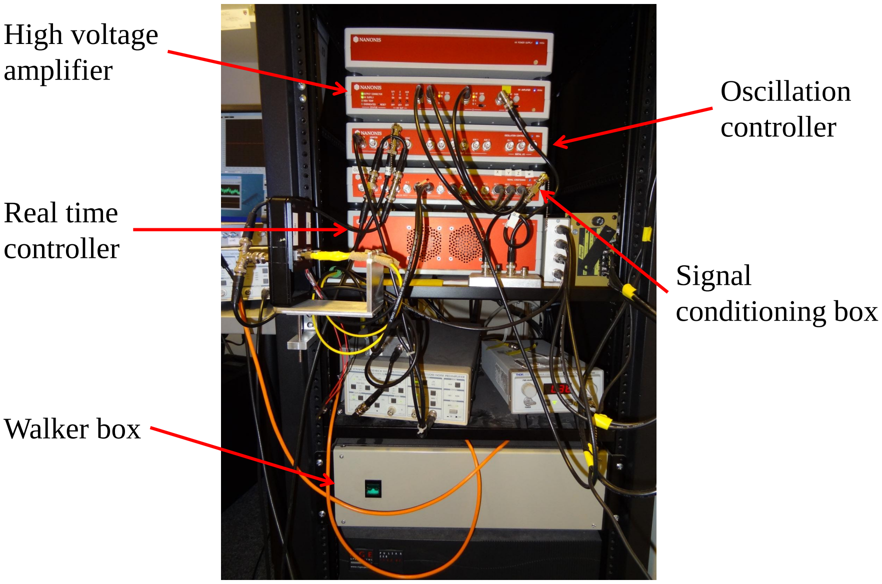

Figure A.5: Photograph of the electronics boxes.

steps at 150 V.

- Exit phase and interferometer feedback (the order does not matter).
- Turn off the drive signal to the shake piezo.
- Ensure that there is sufficient separation between the fiber and cantilever. This means walking the fiber walker until the peak-to-peak interferometer signal no longer changes while continuing to walk, indicating that the cantilever is no longer directly over the fiber.
- Turn off all high voltages.

### A.1.3 Fixing broken connections

Electrical connections can easily break, particularly when disassembling the microscope. The list below provides a rough guide on how to repair these connections.

1. **Identify wires to be connected**

   Locate the connection that has been disconnected. This is often a two-person job, particularly when testing which electrical pin on the microscope head leads to the correct pin on the feedthrough.

2. **Prepare connection for epoxy**

   This is the most difficult task, and can require some creativity. The goal is to connect the two conducting ends in a stable configuration that will not come apart when applying epoxy. Some methods to consider are twisting wires (for connections between two wires), applying Kapton tape near the connection, or bending the wires so they naturally push against the connection to be made.

3. **Prepare EPO-TEK H20E conducting epoxy**

   Prepare a small amount (0.1 g or so) of H20E epoxy on a microscope slide. Do not prepare too small a batch, since variations in the mix ratio result in poor curing.

4. **Apply conducting epoxy to connection**

   Apply a small dab of the epoxy to make the connection.

5. **Cure the epoxy**

   Use a heat lamp to cure the epoxy. In our experience, it has been necessary to move the heat lamp to within a few inches of the connection. It is helpful to use foil to reflect light onto the epoxy. Check the electrical connection periodically to confirm that contact has been made. Note that the epoxy becomes conducting before it fully cures, so make sure the epoxy has hardened before stressing the joint. At 100°C, properly mixed epoxy should cure in 2 hours, and at 120°C, it should cure in 15 minutes. To mitigate the risk of de-poling piezos in the microscope, place a thermometer near the electrical connections to ensure the temperature does not exceed 120°C.

### A.1.4 Z-walker step sizes

We have measured the step size of the z walker for a variety of step voltages at both 295 K and 80 K. We determined the step size by entering feedback in contact mode before and after walking with the z walker. For the 295 K measurements, the scan tube high voltage gain was set to 15, and we used the piezo calibration file “2012_07_17 Room Temp”. For the 80 K measurements, the high voltage gain was set to 40, and we used the piezo calibration file “2012_07_17 77K”. The measured step sizes appear in Table A.1. Note that these step sizes can depend on other factors, such as screw tightness, so the values should be interpreted as a guide.

Table A.1: Z walker step sizes.

| Step Voltage (V) | Step Size at 295 K (nm) | | Step Size at 80 K (nm) | |
|---|---|---|---|---|
| | Forward | Backward | Forward | Backward |
| 100 | 74 | 87 | 37 | 42 |
| 125 | 126 | 148 | 45 | 52 |
| 150 | 174 | 195 | 70 | 80 |
| 175 | 216 | 232 | 100 | 130 |
| 200 | 283 | 296 | 125 | 150 |

### A.1.5 Anomalous shake piezo behavior

From time to time, the shake piezo will stop working, stopping the oscillation of the cantilever. This behavior is most prevalent after working in the experiment room, for example while reassembling the microscope or closing the vacuum can. When the shake piezo stops, the resonance curves appear flat regardless of the shake piezo drive amplitude. Additionally, the interferometer calibration curve will look fine, indicating that the cantilever is still present. To fix the shake piezo, withdraw the cantilever from the sample surface, enter the experiment room, and measure the capacitance between the shake piezo pin and ground. After measuring the appropriate value (0.65 nF), reconnect the shake piezo line and check the resonance once more. For some reason, it appears the act of measuring the capacitance resolves the issue. We don’t have a clear idea of the cause of the problem, but we found the solution while running diagnostic checks when it occurred. We have also noticed that the feedthrough connection for the shake piezo feels loose, so be gentle when removing and reconnecting the shake piezo BNC cable.

# A.2 Vacuum and Cryogenics

## A.2.1 Opening and closing the vacuum can

### Closing the vacuum can

1. **Clean vacuum can and flow cryostat**

   Remove any remaining indium from the previous seal from the sealing edges of the flow cryostat and the vacuum can. This requires looking up at the flow cryostat flange from below. Clean the sealing surface of the vacuum can with a Kimwipe and isopropanol or methanol.

2. **Apply indium to the vacuum can**

   Ideally, indium wire with a diameter of 0.040 inches (1.0 mm) should be used. Determine the length of wire to be used by wrapping the indium around the seal. Cut enough indium to wrap around the seal once with 0.25-0.50 inches to spare. Clean the indium wire with Kimwipes and isopropanol. Coat the wire with a very thin layer of vacuum grease (Dow Corning High Vacuum Grease) by running gloved fingers over the wire to ensure an even coat. This aids in both securing the indium to the vacuum can and removing it after breaking the seal. Apply the seal to the vacuum can, ensuring that the wire is securely pressed into the corner of the sealing surface with equal force all the way around. Be careful not to contaminate the interior of the vacuum can with grease from the seal. The indium seal should be allowed to overlap for approximately 0.1 inches, and the excess should be folded outward. It is convenient for the wire to overlap near a bolt hole, with the excess wire folded out on either side of the hole (Figure A.6).

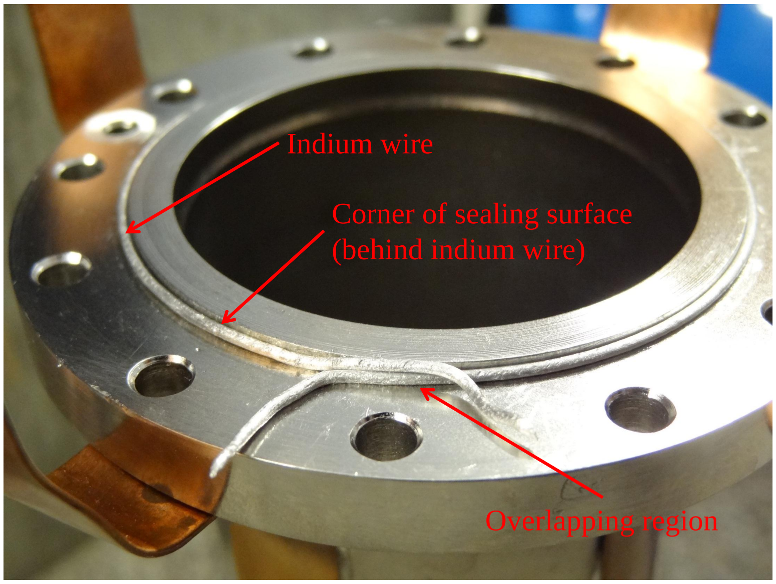

Figure A.6: Photograph depicting indium wire properly applied to the sealing surface of the vacuum can.

3. **Put the microscope in safe mode**

   In addition to the normal safe mode preparations, gently tie back loose wires and the fiber optic cable with Teflon tape to prevent damage while attaching the vacuum can.

4. **Attach the vacuum can**

   Gently slide the vacuum can over the force microscope. Make sure all wires and the fiber optic cable stay inside the vacuum can, as pinching these in the seal will cause significant damage. Once the vacuum can is near the flow cryostat, screw in two screws on opposite sides of the vacuum can, leaving plenty of space between cryostat and the vacuum can. These screws should support the weight of the vacuum can. Screw in the remaining 10 screws. Once the 12 screws have been inserted, confirm that no loose wires are in the space between the vacuum can and the cryostat. Gently lift the vacuum can to make the seal with the cryostat. Note that alignment is critically important! When correctly aligned, the vacuum can appears appears level and the indium makes contact with the entire sealing surface of the cryostat. Test the alignment by tightening the screws. If at any point during tightening the screws become difficult to tighten while there is still visible space between the flanges or the flange spacing is uneven, the alignment needs to be corrected. If this is the case, unscrew all the screws to allow space between the flanges. Attempt to make the seal and tighten the screws once more. Repeat until tightening the screws results in the flanges becoming flush against each other and parallel.

5. **Close vacuum system**

   If any vent ports are open, close them.

6. **Test vacuum seal**

   To test the vacuum seal, turn on the scroll pump by flipping the switch in the experiment room labeled “scroll pump.” If there is no audible leak coming from the indium seal, continue pumping. If an audible leak is present, turn off the scroll pump and vent the vacuum system. Loosen the screws to separate the vacuum can from the cryostat and attempt to make the seal once again.

### Opening the vacuum can

1. **Put the microscope in safe mode**

2. **Prepare the vacuum system**

   Turn off the turbo pump. After the turbo pump has spun down (the rotation should no longer be audible), turn off the scroll pump. Then vent the vacuum system with either dry nitrogen or air. To vent with dry nitrogen, attach a rubber tube from a nitrogen canister to the Swagelok valve in the pumping line near the floor. This valve is between the turbo pump and the scroll pump.

3. **Install plywood boards**

   Form a table under the vacuum can by placing the two plywood boards across the pit. Push them as far against the wall as possible.

4. **Remove screws**

   Remove all screws securing the vacuum can to the flow cryostat using a hex ball screwdriver. Do not use clean tools for this task. The indium seal should secure the vacuum can in place even after the screws have been removed. Place the screws in a container to avoid losing them.

5. **Break indium seal**

   Slide the plywood table sections apart to create a space for the vacuum can to fit when lowering it. Carefully break the indium seal by tilting the vacuum can at a slight angle. While this can require a significant amount of force, it is important to be careful not to damage the microscope by bumping it too severely.

6. **Drop the vacuum can**

   Carefully slide the vacuum can down. Be sure not to bump the microscope head or pull on the loose wires or fiber optic cable. Slide the plywood table sections together after removing the vacuum can.

7. **Remove old indium seal**

   Remove the indium wire from the sealing surfaces of the vacuum can and flow cryostat.

### A.2.2 Pumping down the vacuum system

1. **Close vacuum system**

   Follow appropriate instructions. The microscope should be in safe mode and all high voltages should be off.

2. **Record pressure**

   Start recording pressure in the “PERIPHERALS.vi” window on the peripherals computer.

3. **Turn on scroll pump**

   Flip the switch marked “scroll pump” to turn on the scroll pump. Monitor the pressure.

4. **Turn on the turbo pump**

   Once the pressure drops below 1 Torr, turn on the turbo pump by flipping the switch on the turbo pump controller. If the pressure has not dropped below 1 Torr after an hour, the turbo pump can be turned on if the pressure is below

4 Torr and is monotonically decreasing. If there appear to be occasional spikes in the pressure, continue pumping.

5. **Continue pumping**

   Before turning on any high voltages, continue pumping until the pressure is below $10^{-5}$ Torr. Most experiments can be run while the turbo pump is running. Figure A.7 shows the pressure in the vacuum system versus time for a typical pumpdown.

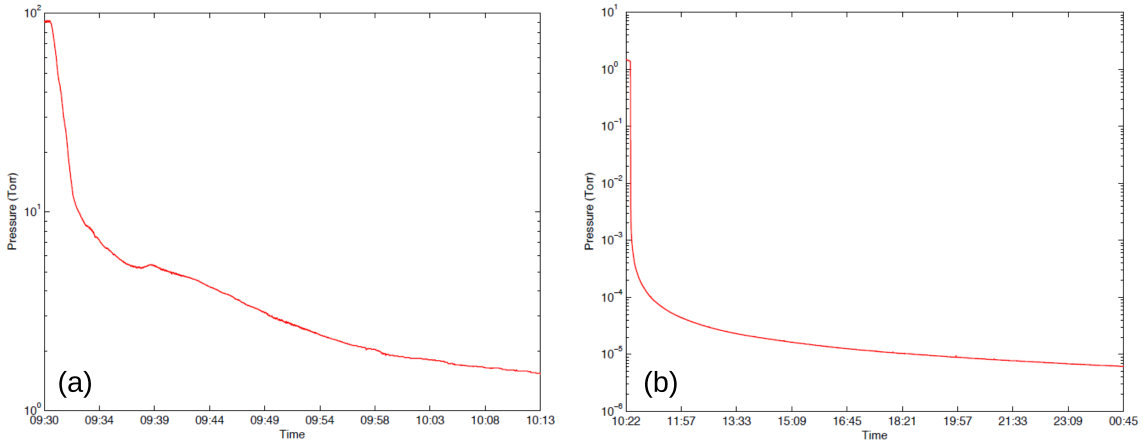

Figure A.7: Pressure of the vacuum system versus time during pump down. The pressure during the initial pump down with the scroll pump is shown in (a). The pressure while pumping down with the turbo pump is shown in (b). Typically, the system can reach $10^{-5}$ Torr within 12 hours. The units of time are in hours:minutes.

### A.2.3 Operating the room and table air springs

#### Floating the experiment room

1. **Put the microscope in safe mode**

2. **Open the valve providing pressurized gas to the air springs**

   Enter the pit and locate the valve controlling air flow to the air spring lines. The valve looks similar to the one depicted in Figure A.8. Open the valve.

3. **Wait for the room to float**

   Wait until sound of air flowing into the air springs is no longer audible (a few minutes).

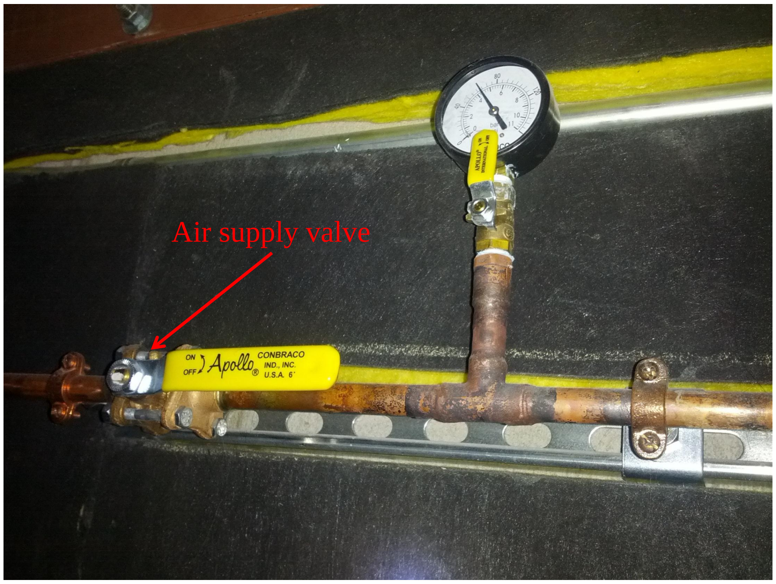

Figure A.8: Photo of a valve responsible for controlling the flow of pressurized gas from the building supply line. One valve controls flow to the room air springs, and another controls flow to the table air springs.

**Un-floating the experiment room**

1. **Put the microscope in safe mode**

2. **Close the valve to the air springs**

   Enter the pit and close the valve to the air supply line for the air springs.

3. **Wait for the air springs to lose pressure**

   This may take several minutes, as there is no way to force air out of the system.

### A.2.4 Floating the experiment table

1. **Put the microscope in safe mode**

2. **Open the valve to the table air springs**

   Enter the pit and locate the valve controlling air flow to the table air spring lines. The valve looks similar to the one depicted in Figure A.8. Open the valve.

3. **Confirm that the table is level**

   If the table is not level, adjust the three threaded rods attached to the air spring valves under the table. These valves control the height of each corner of the table by releasing pressure when the respective corner is above the setpoint determined by the threaded rod. Figure A.9 depicts one of these valves.

4. **Wait for the table to float**

   This happens very quickly (less than a minute).

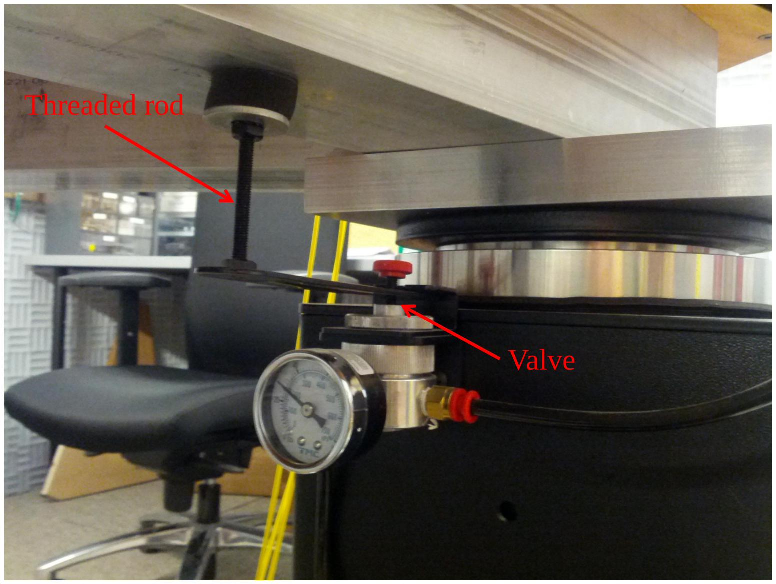

Figure A.9: Photo of a valve responsible for controlling the height of an air spring. The height of the table can be adjusted with the threaded rod.

### A.2.5 Un-floating the experiment table

1. **Put the microscope in safe mode**

2. **Close the valve to the table air springs**

   Enter the pit and close the valve to the air supply line for the air springs.

3. **Release air in the air springs**

   Hasten the process of un-floating the table by sliding the threaded rods out from under the corners of the table. This opens the air spring valves.

4. **Wait for the air springs to lose pressure**

   This happens very quickly (less than a minute).

### A.2.6 Cooling down with liquid nitrogen

1. **Put the microscope in safe mode**

2. **Raise the dewar**

3. **Connect transfer dewar to transfer siphon**

   Attach the liquid nitrogen flex hose to the transfer dewar. Attach the flex hose to the transfer siphon with a rubber hose. Insert the transfer siphon into the transfer siphon port of the experimental dewar and tighten the quick disconnect. Make sure that the transfer line does not touch any delicate items, such as wiring or fiber optic cables.

4. **Open a vent port on the dewar**

   Attach a rubber hose to a free port on the experimental dewar to vent the nitrogen.

5. **Turn on a fan to ventilate the experiment room**

   Suffocation is a danger, as nitrogen displaces oxygen and the experiment room is poorly ventilated.

6. **Transfer nitrogen**

   Transfer nitrogen to desired fill level. To fill the experimental dewar to capacity, transfer until liquid emerges from the vent port.

### A.2.7 Warming up

1. **Ensure vacuum spaces are being pumped**

   While warming up, liquids trapped in the vacuum chamber may rapidly expand. For safety, ensure that the vacuum system is properly pumped or vented.

2. **Lower the dewar**

   See instructions on lowering the dewar. The microscope should be in safe mode, and all high voltages should be off throughout this process.

3. **Allow the system to warm gradually**

   Allow the system to warm gradually while continuing to pump with the turbo pump. Wait until the temperature rises to approximately 150 K at the microscope head.

4. **Turn off the turbo pump**

   Turn off the turbo pump while continuing to pump with the scroll pump. Wait until the temperature rises to approximately 200 K.

5. **Add nitrogen exchange gas**

   Turn off the scroll pump and add a small amount (approximately 100 Torr) of dry nitrogen gas to the system through the Swagelok valve on the pumping line. Use a heat gun to heat the exterior of the vacuum system.

6. **Vent system with dry nitrogen**

   Once the system is near room temperature, vent it with dry nitrogen gas. Wait for both thermometers to stabilize at room temperature before opening the vacuum can.

### A.2.8 Raising and lowering the dewar

The lifting rope has been in place since the microscope was moved to its present location in the LISE building. The rope should be replaced sometime in 2013.

**Raising the dewar**

1. **Put the microscope in safe mode**
2. **Un-float the room and table**
3. **Inspect lifting system**
    - Check the rope, knots, lifting hardware, and lifting lugs on the dewar.
    - Check the condition of the pulleys and that they are securely attached to the experiment table.
    - Check the connection of the rope to the pulley lifting hook.
    - Check that the pulley is securely fastened to the concrete floor at the concrete anchors.
4. **Raise the dewar**

    This task requires two people. One person should operate the hoist, while the other person should sit on the fiberglass floor panels in front of the experiment table. Raise the dewar using the chain hoist. While the dewar is being raised around the flow cryostat, the second person should continuously move the dewar by gently rotating and pushing it. This reduces the likelihood of the dewar catching on any cryostat components, and it provides an early warning to stop raising the dewar if it no longer moves freely. If the dewar does become stuck, lower it until it moves freely again and attempt to raise it again. When the dewar is near the top, rotate the dewar so the threaded rods pass through the corresponding holes in the table. Raise the dewar so it is flush with the table, and secure it in place by attaching nuts to the threaded rods. Release the tension in the lifting system until the ropes are loose.

5. **Float the room and table**

### Lowering the dewar

1. **Put the microscope in safe mode**

2. **Inspect lifting system**

   - Check the rope, knots, lifting hardware, and lifting lugs on the dewar.
   - Check the condition of the pulleys and that they are securely attached to the experiment table.
   - Check the connection of the rope to the pulley lifting hook.
   - Check that the pulley is securely fastened to the concrete floor at the concrete anchors.

3. **Add tension to the lifting system**

   Using the chain hoist, take up slack in the lifting system until the weight of the dewar is primarily supported by the lifting system.

4. **Unscrew support nuts**

   Carefully unscrew the nuts attached to the threaded support rods. The dewar should not move while removing these nuts. If it appears the dewar is moving down while removing the nuts, or if pairs of nuts remain tight while loosening them, add tension to the lifting system.

5. **Lower the dewar**

   This task requires two people. Lower the dewar using the chain hoist. While the dewar is being lowered, the second person should gently rock the dewar to ensure that it does not get stuck on any components of the vacuum system. Continue lowering the dewar until it rests on the cart in the pit and there is no more tension in the system.

6. **Secure metal cap to the dewar**

   Quickly secure the metal cap to the top of the dewar using at least two screws. Installing this cap prevents the buildup of moisture and ice in the dewar.

## A.3 Microscope Maintenance

### A.3.1 Disassembling the microscope

1. **Be careful!**

   Disassembling the microscope is a delicate process during which the microscope may be damaged in a variety of ways. In particular, it is common to crash the cantilever or break the fiber optic cable during the first few attempts. It is also possible to break electrical connections. However, with practice, the procedure becomes second nature and rarely results in damage to the instrument.

2. **Put the microscope in safe mode**

   If necessary, use Teflon-tipped tweezers to remove fiber optic cable from the fiber spool to provide sufficient slack.

3. **Prepare work space**

   Set up the goose neck lamp on the floor of the experiment room behind the microscope. Clean the working area underneath the microscope. To the left of the microscope, place the vice on the 2006-2007 Alfa Aesar catalog wrapped in packing tape. Place the lab jack directly underneath the microscope. See figure A.10 for the correct location of these items relative to the microscope.

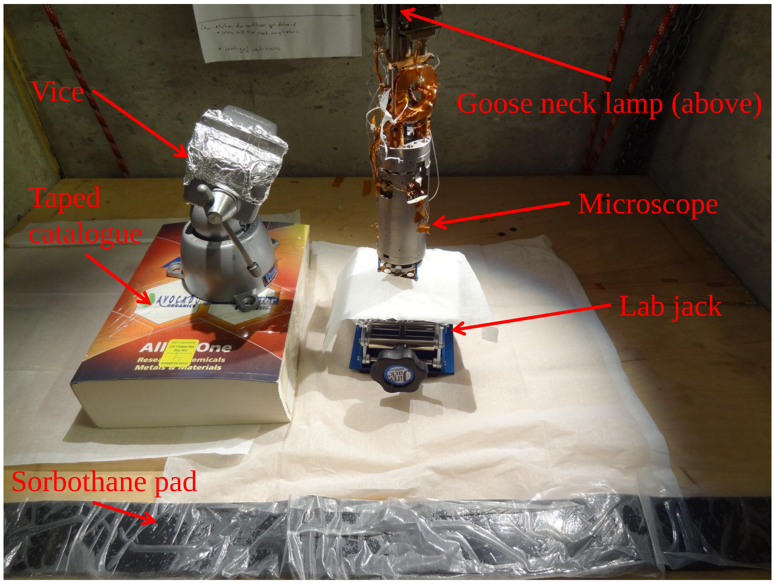

Figure A.10: Photo of a properly organized workspace. The sorbothane pad is useful as an elbow rest while working on the microscope.

4. **Disconnect the force microscope from the titanium support rods**

   Raise the lab jack high enough to lift the microscope to the highest possible position. After raising the microscope, remove the two copper thermal connection blocks on the rear copper support rod. Access the screws holding the blocks in place through the center of the fiber spool. Next, the two blue screws tightening each of the three copper support rods to the titanium rods should be loosened, but not removed. When loose, the copper support rods should slide freely over the titanium rods. The lab jack should then be lowered so the copper support rods are free of the titanium rods. The microscope will tilt to the left as it comes off the titanium rods. Slide the lab jack and microscope slightly to the left, being careful not to stress the optical fiber or wires. See figure A.11 for a photograph depicting the locations of these screws.

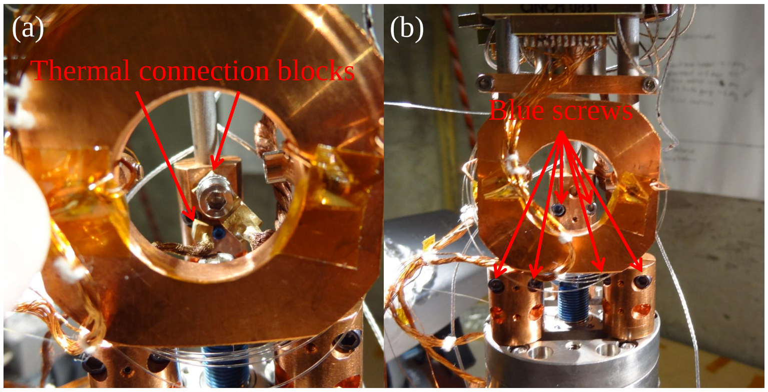

Figure A.11: Photos of the thermal connection blocks (a) and screws fastening the support rods (b).

5. **Remove the cantilever head from the sample head of the microscope**

   Remove the four screws (two #2-56 and two #4-40) securing the cantilever head to the sample head (figure A.12). While doing this, support the cantilever head with a free hand, as it does not balance freely on the sample head. Without support, the cantilever and fiber may crash into the sample surface, possibly damaging all three. After the screws have been removed, without letting go of the cantilever head simultaneously lift and rotate the cantilever head so that the cantilever is facing up. During the rotation, be aware of the location of the wires and the fiber optic cable connected to this part. While it is easy to break the fiber during this procedure, there is no inherent danger in holding the part steady while preparing to rotate it or place it in the vice. Taking this extra time may prevent abrupt motions likely to snap the fiber. Once the cantilever faces up, secure the cantilever head by clamping the rear copper support rod into the vice. For optimal stability, the flat surface of the support rod should be parallel to the surfaces of the vice. The vice can become unstable while supporting the cantilever head, so be sure that the center of mass of the cantilever head is over the base of the vice. Figure A.13 shows the microscope after it has been disassembled.

### A.3.2 Assembling the force microscope

1. **Be careful!**

   The cantilever has been installed and aligned, and the sample has been secured in place. Breaking anything at this stage would be disappointing.

2. **Put the microscope in safe mode**

   In particular, make sure that the cantilever will not crash into the sample while placing the cantilever head back onto the sample head.

3. **Attach the cantilever head to the sample head**

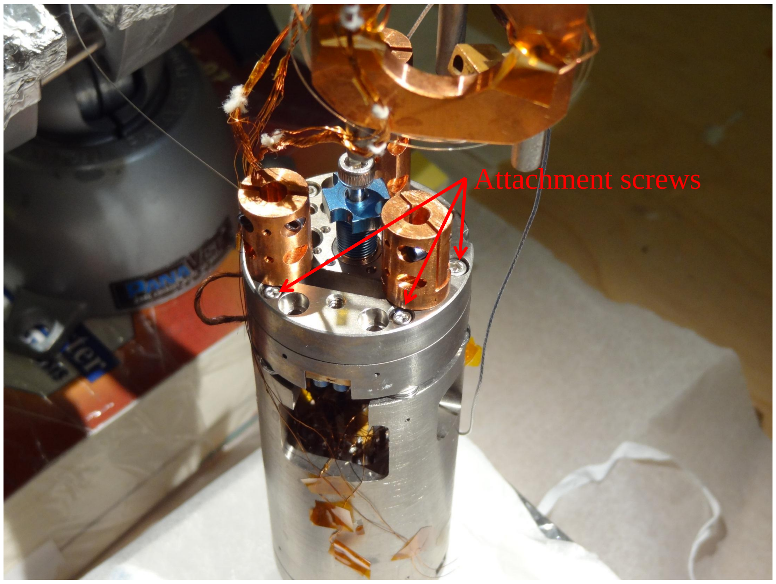

Figure A.12: Photo of the screws used to attach the cantilever head to the sample head.

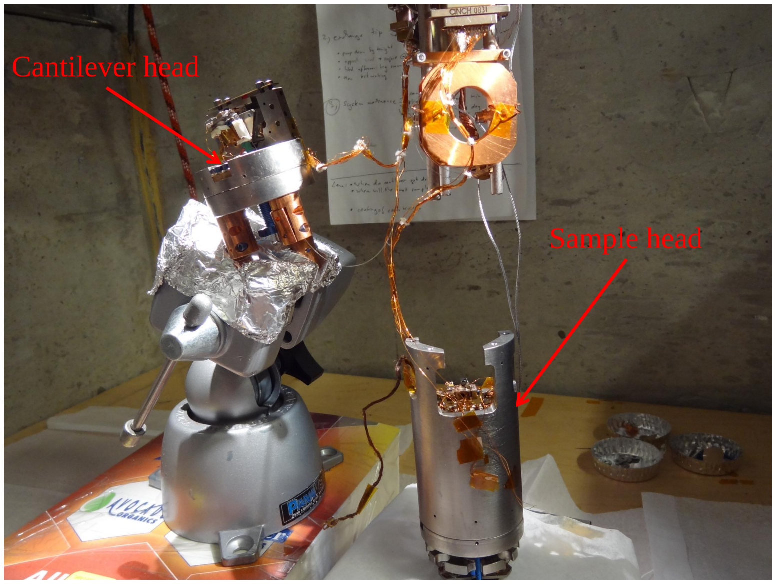

Figure A.13: Photo of the microscope after disassembly.

Remove the cantilever head from the vice and rotate it so the cantilever faces down. Pay attention to the location of the wires and the fiber while rotating. This prevents them from becoming tangled or damaged. While the cantilever head is face down and far from the sample head, insert the four screws into the appropriate clearance holes. Carefully place the cantilever head vertically on the sample head, using the protruding screws as a guide (see figure A.14). Avoid sliding the cantilever head horizontally onto the sample head, as this increases the likelihood of the cantilever crashing. Once the screws make contact with the tapped holes and the cantilever head is flush against the sample head, tighten the screws. Support the cantilever head with one hand while tightening the first screw to prevent crashing the cantilever. Once one screw is tight, there is significantly less danger of a cantilever crash.

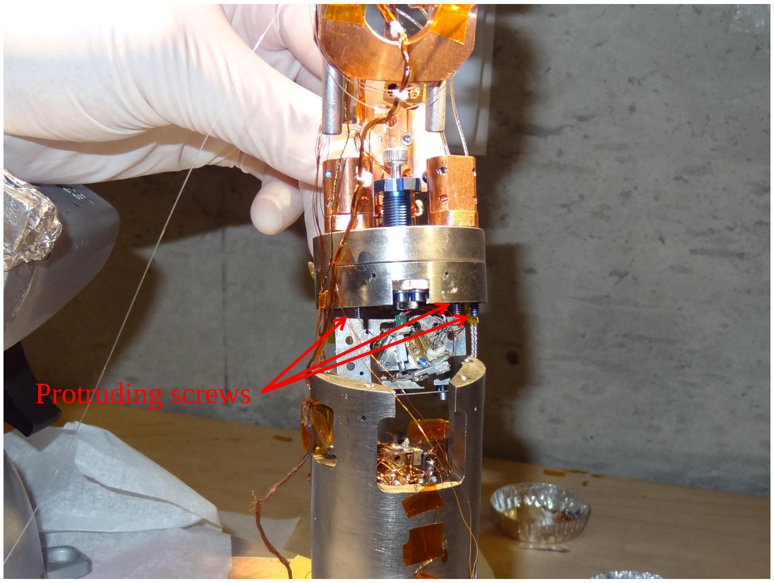

Figure A.14: Photo illustrating reassembly of the microscope. The protruding screws should be used to guide the cantilever head into place. The cantilever head is tilted to make the screws visible; it should be lowered into place parallel to the sample head.

4. **Attach the microscope to the support rods**

   Tightly screw in the copper support rods, then unscrew them less then one turn until the screws face forward. Raise the lab jack so that the copper support rods slide up the titanium rods. Raise the microscope as high as possible, which may require some adjustment of the copper and titanium rods. Once the titanium rods have been fully inserted, tighten the two screws on the face of each copper support rod. Lower the lab jack to confirm that the titanium rods support the weight of the microscope. Remove the lab jack.

### A.3.3 Sample Exchange

1. **Prepare to remove sample**

   The vacuum can should be open. The microscope should be disassembled and in safe mode. The z-walker should be walked high enough to provide easy access to the screw securing the sample mount to the scan tube.

2. **Break the electrical connection to the sample**

   If the sample is electrically connected, break the connection by gently pulling on the wire attached to the sample. As this connection is made with silver paint, the wire should break free easily. If the connection is made with silver epoxy, it may be necessary to cut the wire.

3. **Remove the existing sample**

   Carefully loosen the screw holding the sample mount in place (see Figure A.15). Once the screw is loose, pull it out with tweezers. Avoid dropping the screw into the microscope, as it can be difficult to recover. Remove the sample by gripping the sample mount with tweezers.

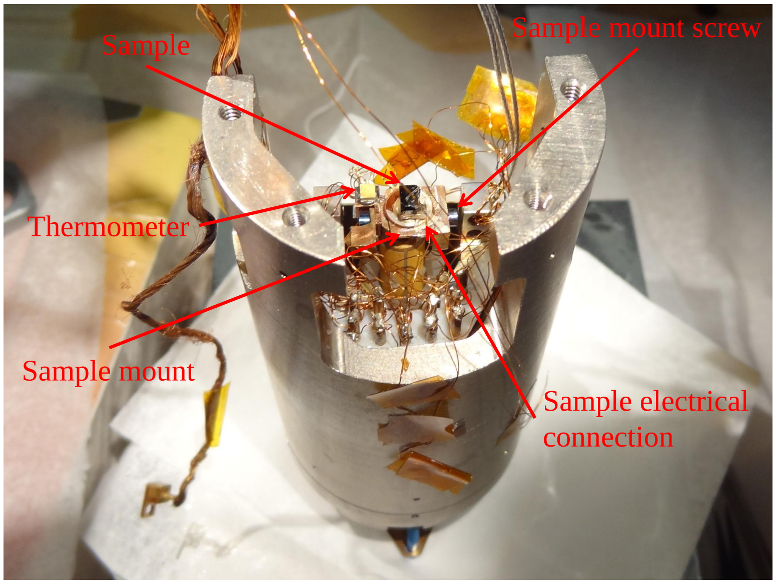

Figure A.15: Photo depicting the sample after proper installation.

4. **Prepare new sample**

   Electrically isolate the sample by securely attaching an insulating material (such as a sapphire disk) to the center of the sample mount with epoxy. Securely attach the sample to the insulating material with epoxy. Check that the sample is level and centered over the sample mount and that future electrical connections to the sample will be straightforward. Ensure that the sample is rigidly attached to the sample mount and that the sample is not electrically connected to the sample mount. The details of this preparation can vary significantly from sample to sample.

5. **Install sample into microscope**

Install the sample by screwing the sample mount into the top of the piezo tube. Figure A.15 illustrates the position of the sample when installed correctly. Be sure that the screw attaching the sample mount to the piezo tube is finger tight. Be careful not to over-tighten the screw! Torquing the screw too hard may damage the scan tube, which would require a great deal of time and effort to replace! Also, ensure that the sample mount does not make contact with the thermometer, which has been an issue for some sample mounts. If this does occur, add a few small washers to the screw between the sample mount and the scan tube, which serves to separate the sample mount from the thermometer.

6. **Make electrical connection to the sample**

   Attach the sample wire to the sample with silver paint. Allow the silver paint to dry completely before checking the electrical connection. The resistance from the electrical feedthrough to the sample joint should be approximately 300 Ω.

### A.3.4 Cleaving and installing the fiber

1. **Prepare to cleave fiber**

   The microscope should be disassembled and in safe mode. Gather the pieces of equipment listed below.

   - Ferrule cleaning wire (ThorLabs model WC100-OD125$\mu$m)
   - Fiber stripper
   - Fiber cleaver
   - Clean metal tweezers

- Clean Teflon-tipped tweezers
- Cutting tweezers

2. **Remove existing fiber and epoxy**

   Cut the fiber near the epoxy securing the fiber below the ferrule. Pull the fiber out of the ferrule with the Teflon-tipped tweezers. Scrape as much existing epoxy from the microscope as possible without causing damage.

3. **Clean ferrule**

   Insert a clean ferrule cleaning wire into the ferrule until it passes fully through the ferrule. The wire is flexible, so use metal tweezers to grip the wire as near to the ferrule as possible. After the wire protrudes through the ferrule, blow it off with canned air to remove broken pieces of optical fiber.

4. **Prepare fiber**

   Remove enough fiber from the spool to operate freely without putting stress on the fiber. Be careful not to break the fiber above the fiber spool, as the fiber can only be replaced by dropping the flow cryostat. This would be a catastrophic setback! Clean the last two inches of the fiber with a Kimwipe soaked in isopropanol.

5. **Strip the fiber**

   Strip approximately 1 inch of the fiber with the fiber stripper. Clean the fiber again with a Kimwipe soaked in isopropanol. Remove the fiber jacket material from the fiber stripper.

6. **Cleave the fiber**

Place the fiber in the fiber cleaver so that the end of stripped region is at the "6" mark on the fiber cleaver. Secure the fiber with the metal clamp and cleave the fiber by pressing the top of the cleaver down.

7. **Check the cleave**

    - Confirm that the laser power is set to 0.35 mW. If this is no longer the case while operating, update the manual.
    - Unplug the reference fiber optic cable from the photodetector.
    - Read the photodetector output from the "DC Interferometer" signal in the Nanonis signal chart. For a good cleave, the photodetector output should be between 750 mV and 800 mV.

8. **Insert fiber into ferrule**

    Push the fiber through the ferrule with the plastic tweezers. The fiber is delicate, so be grip the fiber as close to the ferrule as possible and push gently. Monitor the photodetector output to ensure that it remains around 750 mV. If the signal is lost, the fiber has broken and the ferrule must be cleaned again.

9. **Adjust fiber height**

    This is most easily accomplished with a cantilever installed. Push the fiber up until it is as near the cantilever as possible. In practice, this is usually closer than half the thickness of the die. Test the height by walking the fiber walker while calibrating the interferometer. A minimum peak-to-peak signal of 3 V is a good rule of thumb, but we have been able to achieve signals as high as 7 V.

This number will also depend on the alignment of the cantilever (see cantilever exchange and alignment).

10. **Glue fiber into place**

    Mix a small amount of Torr Seal on a glass slide. Use a dab of the epoxy (approximately the diameter of the fiber) to glue the fiber into place. Cure the epoxy with a heat lamp. At 70°C, the glue cures in one hour. You can test the hardness of the epoxy by inspecting the epoxy remaining on the glass slide.

### A.3.5 Cantilever exchange and alignment

**Remove installed cantilever**

1. **Prepare to remove cantilever**

   The vacuum can should be open. The microscope should be disassembled and in safe mode. The cantilever and fiber should be separated by a large distance to prevent damage to the fiber when removing the cantilever.

2. **Loosen spring plate screws**

   Loosen the screws fastening the spring plate to the cantilever holder until the cantilever is loose. Do not completely remove the screws.

3. **Remove epoxy**

   If the cantilever has been glued to the cantilever holder with epoxy, gently chip it away.

4. **Remove cantilever**

   Remove the cantilever with metal tweezers, being careful not to damage the fiber. Keep the cantilever and label it well, in case it becomes necessary to determine the spring constant at a later time.

### Install new cantilever

1. **Prepare to install cantilever**

   The cantilever and fiber should be separated by a large distance to prevent damage to the fiber when installing the cantilever.

2. **Loosen spring plate screws**

   Loosen the screws fastening the spring plate to the cantilever holder until the cantilever will fit easily in the space between them when lifting the spring plate.

3. **Lift the spring plate**

   Insert the bent tip of the metal tweezers between the spring plate and cantilever holder from behind. Jamming the tweezers in this space is a hands-free method of lifting the spring plate. Confirm that there is enough space to insert the cantilever (see figure A.16). While the tweezers are stuck between the spring plate and cantilever holder, it is still possible to adjust the screws. This is a convenient way of increasing the space between the spring plate and the cantilever holder if the cantilever does not quite fit.

4. **Insert cantilever**

   Insert the cantilever with metal tweezers. Be sure that the tip of the cantilever points up. It is easiest to do this by gripping the die near the cantilever at an approximately 45 degree angle. Be careful not to damage the fiber or cantilever.

Once the cantilever is in the space between the cantilever holder and the spring plate, remove the metal tweezers propping up the spring plate.

5. **Tighten spring plate screws**

   Tighten the screws attaching the spring plate to the cantilever holder. The cantilever should still be loose, so the position can be adjusted with tweezers.

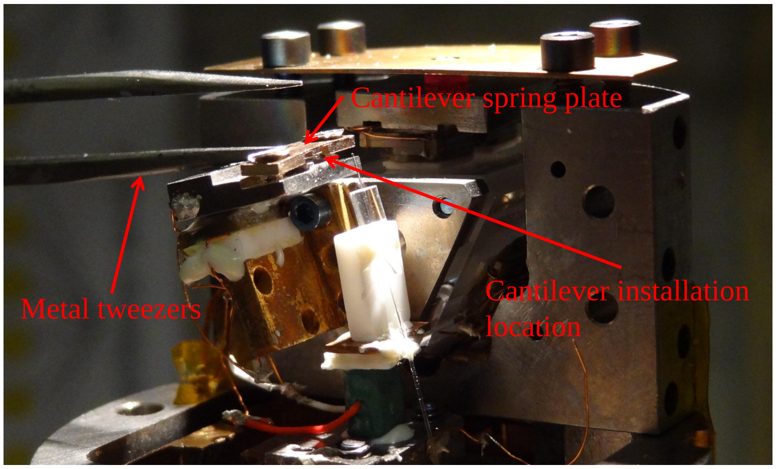

Figure A.16: View of the cantilever head prepared for cantilever installation. The metal tweezers are jammed between the cantilever mounting piece and the spring plate, opening space sufficient to insert the cantilever.

## Align cantilever

1. **Adjust location of the cantilever**

   The cantilever should be laterally positioned so that the fiber is as close to the end of the cantilever as possible. The vertical separation between the cantilever and the fiber should be less than half the width of the cantilever die. Figure A.17 shows a photograph of proper alignment, while figure A.18 provides a schematic view of the adjustments available to align the cantilever.

2. **Tighten the spring plate screws**

   The screws should be tight, but avoid damaging the die. The shape of the resonance curve depends on this tightness, so it may be adjusted during alignment.

3. **Check fiber cleave**

   Unplug the reference fiber optic cable from the photodetector and read the photodetector output from the "DC Interferometer" signal in the Nanonis signal chart. The signal should be larger than 750 mV.

4. **Check interferometer calibration**

   Calibrate the interferometer while walking the fiber walker. Alignment is acceptable if the maximum peak-to-peak signal exceeds 3 V. This is a soft limit. We have achieved signals near 7 V, but have also proceeded if the best result after considerable effort is above 1.5 V or so. The best approach is to make a tradeoff between time spent aligning and the peak signal achieved.

5. **Check resonance curve and phase feedback**

   Check the resonance curve. Apply the settings from the resonance sweep and confirm that the noise level in phase feedback is acceptable. If the resonance curve and noise are unacceptable, attempt re-aligning the cantilever or adjusting the tightness of the spring plate screws.

6. **If necessary, glue cantilever into place**

   In some cases, it may not be possible to optimize screw tightness to obtain an acceptable resonance curve. This is most likely due to mechanical deformation of the spring plate, which would then need to be replaced. A temporary solution is to secure the cantilever into place with a small dot of Torr Seal. Keep in mind that the Torr Seal will need to be chipped away later. The next time the cantilever is replaced, replace the spring plate as well.

7. **Check electrical connection**

   For conducting cantilevers, confirm that the cantilever is electrically connected to the tip pin on the electrical feedthrough. Typically, the resistance between the pin and the cantilever is 300 Ω. If there is no connection, use a small dab of silver paint to connect the cantilever to the cantilever holder.

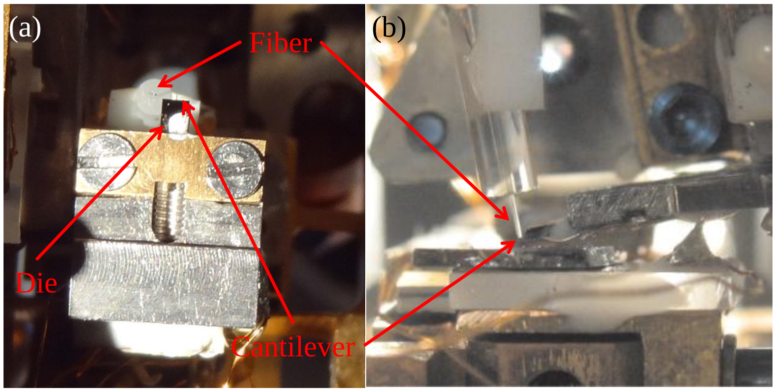

Figure A.17: Top (a) and side (b) view of the fiber and cantilever after alignment. The photo for (b) was taken with the cantilever head already attached to the sample head, but it accurately illustrates the appropriate separation.

# A.4 Microscope Operation

## A.4.1 Checking the interferometer signal

1. **Turn on AUX high voltage**

   At room temperature, use a high-voltage gain setting of 15. At liquid nitrogen

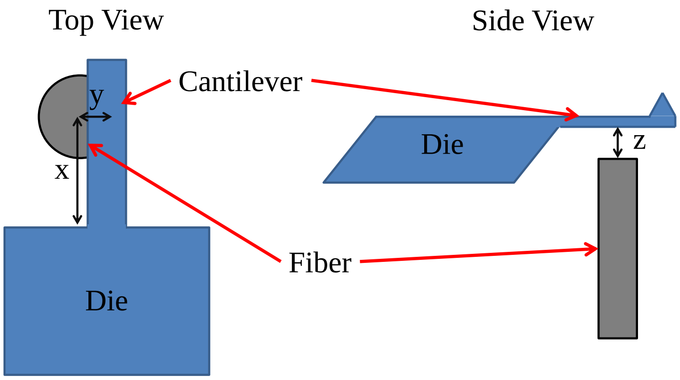

Figure A.18: Diagram of the adjustments available to align the cantilever. The components in the figure are not to scale. Adjust the position of the die in the cantilever to adjust x. Walk with the fiber walker to change y. Adjust z by sliding the fiber through the ferrule.

temperature and below, use a gain setting of 40. This is set on the front panel of the Nanonis high-voltage amplifier.

2. **Turn on interferometer module**

   In the Nanonis software, select the "Interferometer" module.

3. **Select calibrate in the interferometer module**

   Select "Calibrate" from the "Tools" menu, which sweeps the W-piezo voltage and displays the interferometer signal. Slide the bar under the graph so that only a positive voltage is applied to the W-piezo. Figure A.19 shows the interferometer calibration window with an acceptable signal. The manufacturer claims that applying a negative voltage to the W-piezo will damage it, but we have not observed that to be the case.

4. **Search for maximum signal**

   Use the fiber walker to move the fiber continuously until the calibration signal looks like a sine wave. Use a step size of 150 V. When the calibration signal becomes larger, walk by 10 steps at a time. Around the maximum value, walk the fiber walker in the forward and reverse directions to maximize the signal.

5. **Adjust optical attenuator**

   Adjust the attenuator to move the center of the sine wave to 0 V. In practice, it is possible to adjust this within ±50 mV.

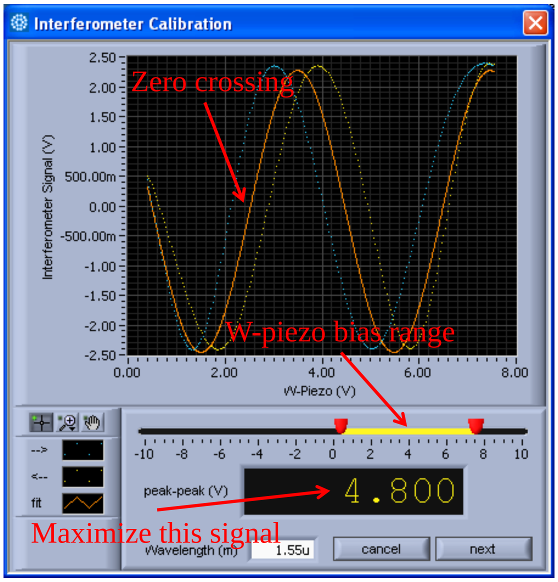

peak-peak (V) 4.800

Wavelength (m) 1.55u

Figure A.19: The interferometer calibration window. The signal amplitude, zero-crossing, and W-piezo voltage range are labeled. The Nanonis software does not update the voltage range with the amplifier setting, so the actual range is -150 V to +150 V.

## A.4.2 Recording a resonance curve

1. **Turn off phase feedback**

   Phase feedback must be off while taking a resonance curve. If it is left on, the phase feedback loop will override the frequency sweep.

2. **Calibrate interferometer**

   Turn on the AUX high-voltage amplifier line. Confirm that the interferometer signal is maximized by translating the cantilever with the fiber walker while the interferometer calibration window is open. Accept the calibration provided by the software.

3. **Turn on interferometer feedback**

4. **Open frequency sweep window in Nanonis**

   In the Oscillation Control module, select "Frequency Sweep" in the "Tools" menu.

5. **Set the anticipated center frequency**

   Set the center frequency $f_{center}$ in the "Phase (deg)" panel of the Oscillation Control module to the nominal value provided by the manufacturer for the installed cantilever.

6. **Set sweep range**

   For the first resonance curve with a new cantilever, use a large frequency range (±20 kHz or more). Set this value in the "Sweep Range" field in the "Frequency Sweep" window.

7. **Turn on the shake piezo drive signal**

   Turn on the "Excitation Signal" in the "Amplitude" panel of the "Oscillation Control" window. In air, use a drive amplitude around 5 mV. In vacuum, use a drive amplitude of 1 mV or less.

8. **Record resonance curve**

   Click the forward arrow button in the “Frequency Sweep” module to obtain a resonance curve.

9. **Save curve and apply settings**

   After finding an acceptable curve, save it. Figure A.20 shows two decent resonant curves, one taken at atmospheric pressure and one in high vacuum. Apply the settings in the “Frequency Sweep” window. The settings must also be applied by selecting “PLL Settings” in the “Tools” menu of the “Oscillation Control” module.

10. **Test phase feedback**

    Turn on phase feedback in the “Oscillation Control” module. Check that the noise level is acceptable. At atmospheric pressure, noise levels of 2 Hz peak-to-peak are common. In vacuum, the noise level should drop to about 0.2 Hz peak-to-peak.

### A.4.3 Approaching the sample

1. **Turn on all high voltages**

2. **Check interferometer settings**

   Confirm that the interferometer has been calibrated and that the interferometer feedback is on.

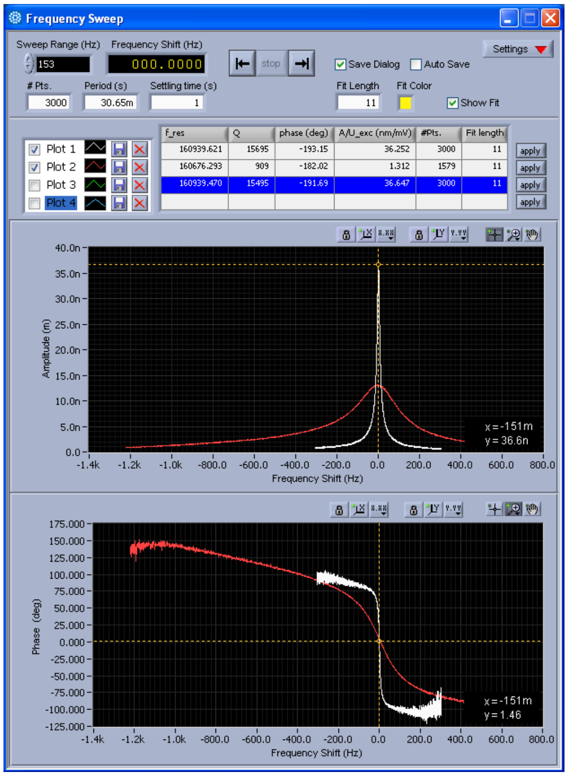

Sweep Range (Hz): 153

Frequency Shift (Hz): 000.0000

☑ Save Dialog ☐ Auto Save

# Pts.: 3000

Period (s): 30.65m

Settling time (s): 1

Fit Length: 11

☑ Show Fit

☑ Plot 1
☑ Plot 2
☐ Plot 3
☐ Plot 4

| f_res | Q | phase (deg) | A/U_exc (nm/mV) | #Pts. | Fit length |
|---|---|---|---|---|---|
| 160939.621 | 15695 | -193.15 | 36.252 | 3000 | 11 |
| 160676.293 | 909 | -182.02 | 1.312 | 1579 | 11 |
| 160939.470 | 15495 | -191.69 | 36.647 | 3000 | 11 |
| | | | | | |

Figure A.20: Screenshot of the "Frequency Sweep" window with two resonance curves shown. The red curve was taken at atmospheric pressure with a 10 mV drive amplitude, and the white curve was taken in high vacuum with a 1 mV drive amplitude. The same cantilever was used in these sweeps.

3. **Record resonance curve and apply the settings**

   See the instructions on how to record a resonance curve.

4. **Choose the desired Z-controller**

   In the "Z-controller" window, select the desired Z-controller. The standard controller is "frequency 2011_03_28", which uses frequency shift as the feedback signal.

5. **Select Z-controller settings**

   For a typical approach, use a setpoint of -4 Hz, time constant of 1 ms, and proportional gain of 100-200 pm/Hz. Adjust the proportional gain to change the speed of the approach.

6. **Turn on safe tip**

   In the "Z-controller" window, turn on the safe tip feature. The safe tip signal should be set to amplitude. Select a threshold of about half the oscillation amplitude. The idea is to protect the tip while minimizing spurious safe tip events, as these stop the approach.

7. **Set walker parameters**

   On the peripherals computer, open the walker controller program. At room temperature, use a step size of 100-150 V, frequency of 10 Hz, 3 steps per trigger, Z-walker relay line, FWD direction, and ext trigger mode. The numbers listed here are conservative, and the step size and number of steps per trigger can be tailored to optimize the speed of the approach. Confirm that the walker box is powered on. Click the "Go" button.

8. **Start approach**

   In the "Auto Approach" window in the Nanonis software, check that the "Number of Pulses" is set to 1. Click the play button to begin the approach.

9. **Monitor approach**

   Confirm that the walker is working by observing the amplitude signal in the signal chart. Each step appears as a spike in the amplitude signal. Open the "Long Term Chart" in Nanonis and monitor the frequency shift signal. This provides information on drift and the stability of feedback, and can indicate that the surface is close.

10. **Auto center the frequency shift**

    When long-range interactions are present, the frequency shift can slowly change while approaching, which may stop the approach. If this occurs, reset the frequency shift to zero by clicking the “auto center” button in the “Phase (deg)” panel of the “Oscillation Controller.”

### A.4.4 Performing a bias spectroscopy measurement

1. **Start with Z-controller in frequency shift feedback**

2. **Lift tip**

   Lift tip approximately 100 nm off the surface.

3. **Turn off shake piezo drive signal**

4. **Calibrate interferometer**

   Follow interferometer calibration instructions. Ensure that the interferometer controller uses a positive slope crosspoint for the feedback signal. Accept the calibration and turn on the interferometer feedback.

5. **Monitor the DC interferometer signal in the long term chart**

6. **Turn the interferometer feedback off**

   Failure to turn off the interferometer feedback will damage the cantilever when entering feedback with the DC interferometer Z-controller.

7. **Switch Z-controller**

   Change the Z-controller to DC interferometer.

8. **Choose setpoint**

   Wait until the drift in the DC interferometer signal on the long term chart becomes stable. This is the "free value" of the DC interferometer signal. Choose a setpoint approximately 100 mV more than this value. For highly reflective samples, a larger value may be required, as the interference fringes from the sample may be large enough to satisfy the feedback criterion even when there is no contact between the cantilever and sample.

9. **Enter feedback with the Z-controller**

10. **Open the "Bias Spectroscopy" module and perform measurements**

### A.4.5 Performing a topographic scan

1. **Enter feedback with the Z-controller**

   Any feedback controller will work. For frequency shift scans, us the "frequency 2011_03_28" controller. For contact-mode scans, use the DC interferometer controller.

2. **Turn on safe tip**

   When imaging with the frequency shift Z-controller, use appropriate safe tip settings to prevent damage to the cantilever.

3. **Select scan parameters in the "Scan Control" window**

   Set the desired scan size, center location, resolution (lines/scan and pixels/line), and scan speed. Type in the desired base name for saving and select whether or not to save the scan when it completes.

4. **Apply tilt correction**

   Select the tilt correction option in the “Scan Control” window.

5. **Begin scanning**

   Press the up or down arrow in the “Scan Control” window to begin scanning.

### A.4.6 Performing a grid spectroscopy scan

1. **Perform bias spectroscopy measurements**

   Follow instructions for bias spectroscopy measurements to determine the desired parameters.

2. **Select grid spectroscopy options**

## A.5 Diagnostic measurements

### A.5.1 Scan tube capacitances

To measure the scan tube capacitances, first set the scan tube location to x=y=z=0, which sets the voltages applied to the scan tube to approximately 0 V. Then, turn off the XY and Z high voltage lines on the front panel of the Nanonis high-voltage amplifier. Unplug the +X, -X, +Y, -Y, and Z BNC cables from the breakout box on the electrical feedthrough. The capacitance measurements should be made between the Z pin and the +X, -X, +Y, and -Y pins on the breakout box. Table A.2 shows the approximate values of the capacitance measured at room temperature and 90K.

Table A.2: The capacitance between the +X, -X, +Y, and -Y electrodes and the Z electrode of the scan piezo.

| Electrode | Capacitance at Room Temperature (nF) | Capacitance at 90K (nF) |
|---|---|---|
| -X | 3.48 | 3.10 |
| +X | 3.42 | 2.96 |
| -Y | 3.51 | 3.00 |
| +Y | 3.60 | 3.14 |

### A.5.2 Walker system capacitances

To measure the walker system capacitances, simply unplug the appropriate 7-pin connector from the breakout box. For safety, ensure that the walker box has been turned off. The capacitance measurements should be made between pins 1-6 of the connectors and pin 7, which is grounded to the walker box (not the vacuum system). Tables A.3, A.4, A.5, and A.6 show the appropriate values of the capacitances for the z walker, fiber walker, x walker, and y walker, respectively. The two fiber walker piezo stacks with low capacitance values at 90K have connections that need repair. The room temperature capacitances reflect correct values at room temperature before the broken connections. The 90K y walker capacitances reflect the fact that the y walker ground pin on the sample head is no longer connected to the y walker ground socket on the 25-pin Cinch connector. This connection must be repaired before operating the y walker. The room temperature y walker capacitances reflect the correct values at room temperature.

Table A.3: Z walker capacitance values.

| Pin | Capacitance at Room Temperature (nF) | Capacitance at 90K (nF) |
|---|---|---|
| 1 | 5.22 | 3.79 |
| 2 | 5.36 | 3.94 |
| 3 | 5.09 | 3.75 |
| 4 | 5.24 | 3.87 |
| 5 | 5.04 | 3.67 |
| 6 | 4.93 | 3.64 |

Table A.4: Fiber walker capacitance values. Two fiber walker piezo stack connections need repair.

| Pin | Capacitance at Room Temperature (nF) | Capacitance at 90K (nF) |
|---|---|---|
| 1 | 2.48 | 0.20 |
| 2 | 2.98 | 2.20 |
| 3 | 2.47 | 0.25 |
| 4 | 2.46 | 1.84 |
| 5 | 2.52 | 1.92 |
| 6 | 2.92 | 2.19 |

Table A.5: X walker capacitance values.

| Pin | Capacitance at Room Temperature (nF) | Capacitance at 90K (nF) |
|---|---|---|
| 1 | 4.12 | 3.16 |
| 2 | 4.25 | 3.30 |
| 3 | 4.14 | 3.19 |
| 4 | 4.30 | 3.31 |
| 5 | 5.00 | 3.70 |
| 6 | 4.20 | 3.18 |

Table A.6: Y walker capacitance values. Presently, the y walker ground line needs to be repaired.

| Pin | Capacitance at Room Temperature (nF) | Capacitance at 90K (nF) |
|---|---|---|
| 1 | 4.17 | 0.25 |
| 2 | 4.19 | 0.24 |
| 3 | 4.35 | 0.24 |
| 4 | 4.60 | 0.25 |
| 5 | 4.29 | 0.24 |
| 6 | 4.09 | 0.24 |

### A.5.3 Other capacitances

There are two other important piezoelectric elements in the system, the shake piezo and the W piezo. Before unplugging the W piezo BNC cable from the breakout box, turn off the AUX high voltage line on the front panel of the Nanonis high-voltage amplifier. The capacitances for these piezos should be measured between the center pin of the appropriate BNC connector and ground. For these measurements, it is easiest to use anywhere on the vacuum system as the ground connection. The capacitances measured at room temperature and 90K appear in Table A.7

Table A.7: Shake piezo and W piezo capacitance values.

| Piezo | Capacitance at Room Temperature (nF) | Capacitance at 90K (nF) |
|---|---|---|
| Shake Piezo | 0.65 | 0.39 |
| W Piezo | 92 | 15.8 |

# Appendix B

# Operating Checklists for Experienced Users

## B.1 Approach

- All necessary high voltages on (scan piezo, walker box)
- Confirm walker settings
  - Voltage
  - Number of steps
  - Direction
  - Walker axis (relay line)
- Update oscillation control to settings from recent resonance curve
- Check Z-controller setpoint and feedback parameters

- Check speed of approach
- Apply safe tip

## B.2 Pre-scan

- Check resonance curve
- Take force-distance curve
- Check tilt control
- Check feedback settings
- Check tip bias (CPD)
- Check safe tip
- Check scan settings
  - Speed
  - Resolution
  - Saved channels

## B.3 Opening the vacuum can

- Walk back to a safe distance
- Turn off all high voltages

- Turn turbo pump off and wait 5 min
- Turn scroll pump off
- Vent after turbo has spun down
- Open vacuum can

## B.4 Reassembling the microscope

- Check reflected signal from fiber
- Cantilever
    - Tighten screws
    - Check resonance
    - Magnetize, if necessary
- Sample
    - Clean
    - Mechanically secure
    - Electrically connected (and not shorted)
- Check that there will be sufficient sample-cantilever separation during assembly
- Screw cantilever head to sample head
- Attach to posts
- Attach thermal connection blocks, if necessary

## B.5 Closing the vacuum can and pumping down

- Cantilever
  - Check position over sample
  - Check resonance
- Walk back to a safe distance
- Turn off all high voltages
- Close the vacuum can
- Turn on the scroll pump
- After the pressure is below 1 Torr, turn on the turbo pump
- High voltages can be turned on once the pressure is below $10^{-5}$ Torr
- Check resonance once pressure is sufficiently low (below $10^{-5}$ Torr)

## B.6 Set up contact-mode bias spectroscopy

- Check topography
  - Z-controller set to feed back on frequency shift
  - Shake piezo drive turned on
  - Appropriate feedbacks turned on (interferometer, phase, z-controller)
- Check bias spectroscopy

  - Withdraw tip approximately 100 nm
  - Turn off phase feedback
  - **Turn off interferometer feedback. Forgetting to do this may result in catastrophic damage to the cantilever**
  - Note free value of the DC interferometer signal after the initial drift subsides
  - Switch to the DC interferometer z-controller with a setpoint equal to the DC interferometer free value plus 50-100 mV (this will depend on the peak-to-peak value of the interferometer calibration curve)
  - Enter z-controller feedback
  - Take bias spectroscopy measurements to test and determine desired parameters

- Test grid spectroscopy on a 4x4 grid with test points at corners of desired scan frame
- Set up grid spectroscopy with desired resolution

# Bibliography

[1] M. A. Al-Khafaji, D. G. R. Jones, W. M. Rainforth, M. R. J. Gibbs, H. A. Davies, and I. R. Harris. Magnetic force imaging of domain structures for a (Pr/Nd)FeB alloy. *Journal of Applied Physics*, 83(5):2715–2718, 1998.

[2] T. R. Albrecht, P. Grutter, D. Horne, and D. Rugar. Frequency modulation detection using high-Q cantilevers for enhanced force microscope sensitivity. *Journal of Applied Physics*, 69(2):668, 1991.

[3] Philip B. Allen, Renata M. Wentzcovitch, Werner W. Schulz, and Paul C. Canfield. Resistivity of the high-temperature metallic phase of VO2. *Physical Review B*, 48(7):4359–4363, 1993.

[4] G. Binnig, C. F. Quate, and Ch. Gerber. Atomic force microscope. *Physical Review Letters*, 56(9):930–934, 1986.

[5] P. P. Boriskov, A. A. Velichko, A. L. Pergament, G. B. Stefanovich, and D. G. Stefanovich. The Effect of Electric Field on Metal-Insulator Phase Transition in Vanadium Dioxide. *Technical Physics Letters*, 28(5):406–408, 2002.

[6] F. D. Callaghan, X. Yu, and C. J. Mellor. Variable temperature magnetic force

microscopy with piezoelectric quartz tuning forks as probes optimized using Q-control. *Applied Physics Letters*, 87(21):214106, 2005.

[7] A. Cavalleri, Th. Dekorsy, H. H. W. Chong, J. C. Kieffer, and R. W. Schoenlein. Evidence for a structurally-driven insulator-to-metal transition in VO2: A view from the ultrafast timescale. *Physical Review B*, 70(16):161102(R), October 2004.

[8] W. D. Corner and M. J. Hawton. Magneticd Domains and Domain Wall Energies in Rare Earth-Iron-Boron Intermetallics. *Journal of Magnetism and Magnetic Materials*, 72:59–66, 1988.

[9] U. Durig, O. Zuger, and A. Stalder. Interaction force detection in scanning probe microscopy: Methods and applications. *Journal of Applied Physics*, 72(5):1778–1798, 1992.

[10] A. Frenzel, M. M. Qazilbash, M. Brehm, Byung-Gyu Chae, Bong-Jun Kim, Hyun-Tak Kim, A. V. Balatsky, F. Keilmann, and D. N. Basov. Inhomogeneous electronic state near the insulator-to-metal transition in the correlated oxide VO2. *Physical Review B*, 80(11):115115, September 2009.

[11] Gokul Gopalakrishnan, Dmitry Ruzmetov, and Shriram Ramanathan. On the triggering mechanism for the metalinsulator transition in thin film VO2 devices: electric field versus thermal effects. *Journal of Materials Science*, 44(19):5345–5353, April 2009.

[12] Ihsan Gunev, Aydin Varol, Sertac Karaman, and Cagatay Basdogan. Adaptive

Q control for tapping-mode nanoscanning using a piezoactuated bimorph probe. *Review of Scientific Instruments*, 78(4):043707, April 2007.

[13] R. Held, T. Vancura, T. Heinzel, K. Ensslin, M. Holland, and W. Wegscheider. In-plane gates and nanostructures fabricated by direct oxidation of semiconductor heterostructures with an atomic force microscope. *Applied Physics Letters*, 73(2):262–264, 1998.

[14] J. Herbst. R2Fe14B materials: Intrinsic properties and technological aspects. *Reviews of Modern Physics*, 63(4):819–898, 1991.

[15] Jan F. Herbst, John J. Croat, and Frederick E. Pinkerton. Relationships between crystal structure and magnetic properties in Nd_{2}Fe_{14}B. *Physical Review B*, 29(7):4176–4178, April 1984.

[16] H. Holscher, D. Ebeling, and U. D. Schwarz. Theory of Q-Controlled dynamic force microscopy in air. *Journal of Applied Physics*, 99(8):084311, 2006.

[17] Rainer D. Jaggi, Alfredo Franco-Obregon, Paul Studerus, and Klaus Ensslin. Detailed analysis of forces influencing lateral resolution for Q-control and tapping mode. *Applied Physics Letters*, 79(1):135–137, 2001.

[18] Hyun-Tak Kim, Yong Wook Lee, Bong-Jun Kim, Byung-Gyu Chae, Sun Jin Yun, Kwang-Yong Kang, Kang-Jeon Han, Ki-Ju Yee, and Yong-Sik Lim. Monoclinic and Correlated Metal Phase in VO2 as Evidence of the Mott Transition: Coherent Phonon Analysis. *Physical Review Letters*, 97(26):266401, December 2006.

[19] Jeehoon Kim, Changhyun Ko, Alex Frenzel, Shriram Ramanathan, and Jennifer E. Hoffman. Nanoscale imaging and control of resistance switching in VO[sub 2] at room temperature. *Applied Physics Letters*, 96(21):213106, 2010.

[20] Changhyun Ko and Shriram Ramanathan. Observation of electric field-assisted phase transition in thin film vanadium oxide in a metal-oxide-semiconductor device geometry. *Applied Physics Letters*, 93(25):252101, 2008.

[21] Changhyun Ko, Zheng Yang, and Shriram Ramanathan. Work Function of Vanadium Dioxide Thin Films Across the Metal-Insulator Transition and the Role of Surface Nonstoichiometry. *ACS Applied Materials & Interfaces*, 3(9):3396–3401, September 2011.

[22] Naritaka Kobayashi, Yan Jun Li, Yoshitaka Naitoh, Masami Kageshima, and Yasuhiro Sugawara. Theoretical investigation on force sensitivity in Q-controlled phase-modulation atomic force microscopy in constant-amplitude mode. *Journal of Applied Physics*, 103(5):054305, 2008.

[23] Janos Kokavecz, Zoltan L. Horvath, and Adam Mechler. Dynamical properties of the Q-controlled atomic force microscope. *Applied Physics Letters*, 85(15):3232–3234, 2004.

[24] A. Kreyssig, R. Prozorov, C. D. Dewhurst, P. C. Canfield, R. W. McCallum, and A. I. Goldman. Probing Fractal Magnetic Domains on Multiple Length Scales in Nd2Fe14B. *Physical Review Letters*, 102(4):047204, January 2009.

[25] R. T. Rajendra Kumar, B. Karunagaran, D. Mangalaraj, Sa. K. Narayandass,

P. Manoravi, M. Joseph, and Vishnu Gopal. Pulsed laser deposited vanadium oxide thin films for uncooled infrared detectors. *Sensors and Actuators A*, 107:62–67, October 2003.

[26] S. Masubuchi, M. Ono, K. Yoshida, K. Hirakawa, and T. Machida. Fabrication of graphene nanoribbon by local anodic oxidation lithography using atomic force microscope. *Applied Physics Letters*, 94(8):082107, 2009.

[27] D. Maurer and A. Leue. Investigation of transition metal oxides by ultrasonic microscopy. *Materials Science and Engineering: A*, 370:440–443, April 2004.

[28] J Mertz and O Marti. Regulation of a microcantilever response by force feedback. *Applied Physics Letters*, 62(19):2344–2346, 1993.

[29] E Meyer. Atomic Force Microscopy. *Progress in Surface Science*, 41:3–49, 1992.

[30] F. J. Morin. Oxides which show a metal-to-insulator transition at the Neel temperature. *Physical Review Letters*, 3(1):34–36, 1959.

[31] Joyeeta Nag and R. F. Haglund Jr. Synthesis of vanadium dioxide thin films and nanoparticles. *Journal of Physics: Condensed Matter*, 20(26):264016, July 2008.

[32] Joyeeta Nag, Richard F. Haglund Jr., E. Andrew Payzant, and Karren L. More. Non-congruence of Thermally Driven Structural and Electronic Transitions in VO2. *arXiv*, March 2010.

[33] J. Narayan and V. M. Bhosle. Phase transition and critical issues in structure-property correlations of vanadium oxide. *Journal of Applied Physics*, 100(10):103524, 2006.

[34] Kunio Okimura, Joe Sakai, and Shriram Ramanathan. In situ x-ray diffraction studies on epitaxial VO[sub 2] films grown on c-Al[sub 2]O[sub 3] during thermally induced insulator-metal transition. *Journal of Applied Physics*, 107(6):063503, 2010.

[35] Bilal Orun, Serkan Necipoglu, Cagatay Basdogan, and Levent Guvenc. State feedback control for adjusting the dynamic behavior of a piezoactuated bimorph atomic force microscopy probe. *Review of Scientific Instruments*, 80(6):063701, June 2009.

[36] Yu. G. Pastushenkov. Some Features of Magnetic Domain Structure Reorganization during Spin-Reorientation Phase Transitions of the First and Second Order. *Bulletin of the Russian Academy of Sciences: Physics*, 74(10):1423–1425, November 2010.

[37] Yu. G. Pastushenkov, A. Forkl, and H. Kronmuller. Temperature dependence of the domain structure in Fe14Nd2B single crystals during the spin-reorientation transition. *Journal of Magnetism and Magnetic Materials*, 174:278–288, 1997.

[38] J. P. Pouget, H. Launois, J. P. D'Haenens, P. Merenda, and T. M. Rice. Electron Localization Induced by Uniaxial Stress in Pure VO2. *Physical Review Letters*, 35(13):873–875, 1975.

[39] M. M. Qazilbash, M. Brehm, Byung-Gyu Chae, P.-C. Ho, G. O. Andreev, Bong-Jun Kim, Sun Jin Yun, A. V. Balatsky, M. B. Maple, F. Keilmann, Hyun-Tak Kim, and D. N. Basov. Mott transition in VO2 revealed by infrared spectroscopy and nano-imaging. *Science*, 318(5857):1750–1753, December 2007.

[40] M. M. Qazilbash, J. J. Hamlin, R. E. Baumbach, Lijun Zhang, D. J. Singh, M. B. Maple, and D. N. Basov. Electronic correlations in the iron pnictides. *Nature Physics*, 5(9):647–650, July 2009.

[41] M. M. Qazilbash, A. Tripathi, A. A. Schafgans, Bong-Jun Kim, Hyun-Tak Kim, Zhonghou Cai, M. V. Holt, J. M. Maser, F. Keilmann, O. G. Shpyrko, and D. N. Basov. Nanoscale imaging of the electronic and structural transitions in vanadium dioxide. *Physical Review B*, 83(16):165108, April 2011.

[42] W. R. Roach. Holographic Storage in VO2. *Applied Physics Letters*, 19(11):453–455, 1971.

[43] Tomas R. Rodriguez and Ricardo Garcia. Theory of Q control in atomic force microscopy. *Applied Physics Letters*, 82(26):4821–4823, 2003.

[44] Leif Roschier, Jari Penttila, Michel Martin, Pertti Hakonen, Mikko Paalanen, Unto Tapper, Esko I. Kauppinen, Catherine Journet, and Patrick Bernier. Single-electron transistor made of multiwalled carbon nanotube using scanning probe manipulation. *Applied Physics Letters*, 75(5):728–730, 1999.

[45] D. Rugar and P. Grutter. Mechanical parametric amplification and thermomechanical noise squeezing. *Physical Review Letters*, 67(6):699–702, 1991.

[46] Dmitry Ruzmetov, Don Heiman, Bruce B. Claflin, Venkatesh Narayanamurti, and Shriram Ramanathan. Hall carrier density and magnetoresistance measurements in thin-film vanadium dioxide across the metal-insulator transition. *Physical Review B*, 79(15):153107, 2009.

[47] Deepak R. Sahoo, De Tathagata, and Murti V. Salapaka. Observer based imaging methods for Atomic Force Microscopy. *Proceedings of the 44th IEEE Conference on Decision and Control*, pages 1185–1190, 2005.

[48] John G. Simmons. Poole-Frenkel Effect and Schottky Effect in Metal-Insulator-Metal Systems. *Physical Review*, 155(3):657–660, March 1967.

[49] T. Sulchek, R. Hsieh, J. D. Adams, G. G. Yaralioglu, S. C. Minne, C. F. Quate, J. P. Cleveland, A. Atalar, and D. M. Adderton. High-speed tapping mode imaging with active Q control for atomic force microscopy. *Applied Physics Letters*, 76(11):1473–1475, 2000.

[50] Witold Szmaja. Investigations of the domain structure of anisotropic sintered NdFeB-based permanent magnets. *Journal of Magnetism and Magnetic Materials*, 301(2):546–561, June 2006.

[51] Javier Tamayo, Andrew D. L. Humphris, and Mervyn J. Miles. Piconewton regime dynamic force microscopy in liquid. *Applied Physics Letters*, 77(4):582–584, 2000.

[52] Cédric Weber, David D. ORegan, Nicholas D. M. Hine, Mike C. Payne, Gabriel Kotliar, and Peter B. Littlewood. Vanadium Dioxide: A Peierls-Mott Insulator Stable against Disorder. *Physical Review Letters*, 108(25):256402, June 2012.

[53] David M. Weld and Aharon Kapitulnik. Feedback control and characterization of a microcantilever using optical radiation pressure. *Applied Physics Letters*, 89(16):164102, 2006.

[54] Joachim Welker and Franz J. Giessibl. Revealing the Angular Symmetry of Chemical Bonds by Atomic Force Microscopy. *Science*, 336(6080):444–449, April 2012.

[55] B. Wu, A. Zimmers, H. Aubin, R. Ghosh, Y. Liu, and R. Lopez. Electric-field-driven phase transition in vanadium dioxide. *Physical Review B*, 84(24):241410(R), December 2011.

[56] Z. Yang, C. Ko, and S. Ramanathan. Metal-insulator transition characteristics of VO[sub 2] thin films grown on Ge(100) single crystals. *Journal of Applied Physics*, 108(7):073708, 2010.

[57] Zheng Yang, Sean Hart, Changhyun Ko, Amir Yacoby, and Shriram Ramanathan. Studies on electric triggering of the metal-insulator transition in VO2 thin films between 77 K and 300 K. *Journal of Applied Physics*, 110(3):033725, 2011.

[58] Zheng Yang, Changhyun Ko, Viswanath Balakrishnan, Gokul Gopalakrishnan, and Shriram Ramanathan. Dielectric and carrier transport properties of vanadium dioxide thin films across the phase transition utilizing gated capacitor devices. *Physical Review B*, 82(20):205101, November 2010.

[59] Zheng Yang, You Zhou, and Shriram Ramanathan. Studies on room-temperature electric-field effect in ionic-liquid gated VO2 three-terminal devices. *Journal of Applied Physics*, 111(1):014506, 2012.